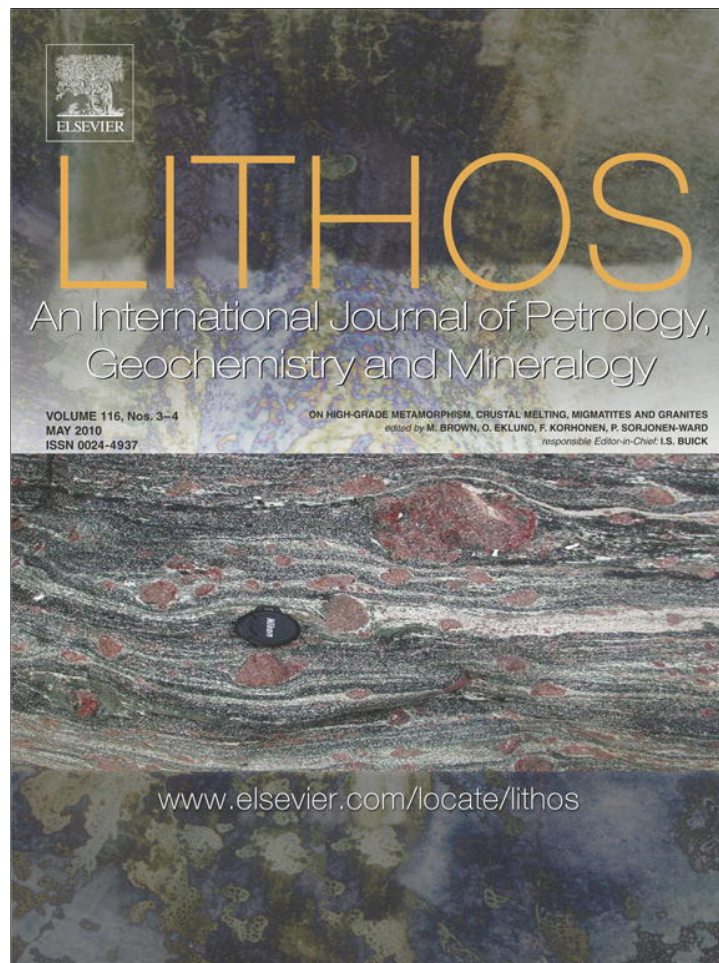


Provided for non-commercial research and education use.  
Not for reproduction, distribution or commercial use.



This article appeared in a journal published by Elsevier. The attached copy is furnished to the author for internal non-commercial research and education use, including for instruction at the authors institution and sharing with colleagues.

Other uses, including reproduction and distribution, or selling or licensing copies, or posting to personal, institutional or third party websites are prohibited.

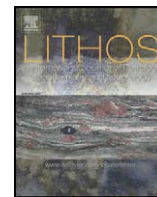
In most cases authors are permitted to post their version of the article (e.g. in Word or Tex form) to their personal website or institutional repository. Authors requiring further information regarding Elsevier's archiving and manuscript policies are encouraged to visit:

<http://www.elsevier.com/copyright>



Contents lists available at ScienceDirect

Lithos

journal homepage: [www.elsevier.com/locate/lithos](http://www.elsevier.com/locate/lithos)

## Hybridization of granitic magmas in the source: The origin of the Karakoram Batholith, Ladakh, NW India

H. Reichardt<sup>a,\*</sup>, R.F. Weinberg<sup>a</sup>, U.B. Andersson<sup>b</sup>, C.M. Fanning<sup>c</sup>

<sup>a</sup> School of Geosciences, Monash University, Clayton, VIC 3800, Australia

<sup>b</sup> Laboratory for Isotope Geology, Swedish Museum for Natural History, Box 50007, SE-104 05 Stockholm, Sweden

<sup>c</sup> Research School of Earth Sciences, The Australian National University, Mills Road, Canberra ACT 0200, Australia

### ARTICLE INFO

#### Article history:

Received 17 April 2009

Accepted 22 November 2009

Available online 2 December 2009

#### Keywords:

Karakoram Shear Zone

Karakoram Batholith

Crustal anatexis

Magma mixing

Radiogenic isotopes

### ABSTRACT

Many magmatic bodies have a hybrid isotopic signature suggesting that somewhere during genesis, transport and emplacement, magmas assimilated other rocks or mixed with other magmas. Where and how hybridization takes place is seldom documented. Here, we investigate a magmatic system in the Eastern Karakoram, Ladakh, NW India, comprising an anatectic zone, and a network of sheets, stocks and plutons exposed in the Pangong Metamorphic Complex within the Karakoram Shear Zone, as well as the Karakoram Batholith. These granitic rocks have an isotopic signature indicative of a mixture between mantle and crustal sources. In the anatectic region, calc-alkaline granitoids and their meta-sedimentary country rocks underwent water-fluxed partial melting at upper amphibolite facies between 20 and 14 Ma ago. Anatexis gave rise to leucosomes and intrusive rocks that have a range in composition from leucotonalite to leucogranite. Those related to the partial melting of calc-alkaline rocks contain hornblende, whereas those related to Bt-psammites contain two micas ± garnet. Leucosomes rooting in different source rocks merge with each other and homogenize as they link up to form a hierarchy of magma channels, feeding into stocks, plutons and ultimately into the Karakoram Batholith. This interpretation is supported by Sr and Nd isotopes. Initial  $^{87}\text{Sr}/^{86}\text{Sr}$  and  $\epsilon_{\text{Nd}}$  values are distinct for each of the magma protoliths in the anatectic zone and for the magmatic products. Calc-alkaline granitoids have initial  $^{87}\text{Sr}/^{86}\text{Sr} = 0.7042$  to  $0.7077$  and  $\epsilon_{\text{Nd}} = +0.6$  to  $+2.4$ , indicative of a slightly depleted mantle source region. This is in contrast to the meta-sedimentary rocks that yield initial  $^{87}\text{Sr}/^{86}\text{Sr} = 0.7115$  to  $0.7161$  and  $\epsilon_{\text{Nd}} = -10.0$  to  $-9.6$ , suggesting a stronger crustal component. Leucogranitic rocks, including a variety of leucosomes in the anatectic zone and samples from the Karakoram Batholith, yield intermediate values of initial  $^{87}\text{Sr}/^{86}\text{Sr} = 0.7076$  to  $0.7121$  and  $\epsilon_{\text{Nd}} = -3.6$  to  $-7.1$  that can be modelled by mixing of the two source rocks. The hybrid signature of leucosomes and their similarity to intrusive leucogranites indicate that magma hybridization must have taken place within the source region as a result of the confluence of magmas to form the escape channels. We conclude that the voluminous leucogranites of the Miocene Karakoram Batholith result from water-fluxed intracrustal melting of sources with crustal and mantle signatures, and that mixing occurred within the source.

© 2009 Elsevier B.V. All rights reserved.

### 1. Introduction

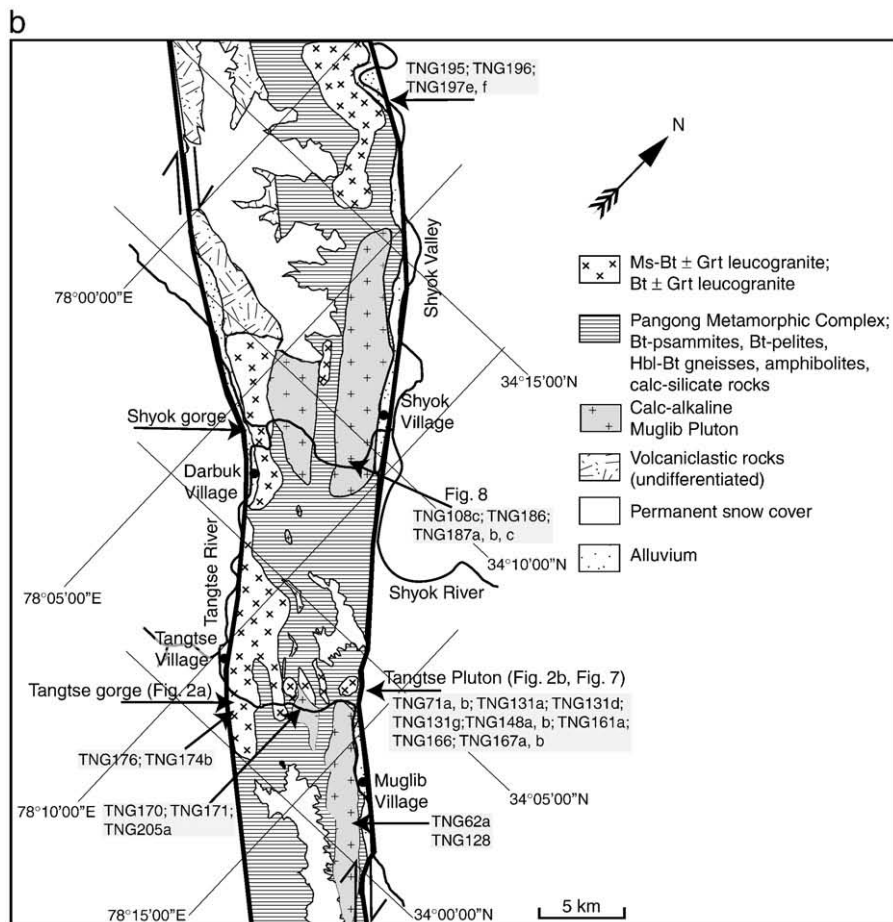
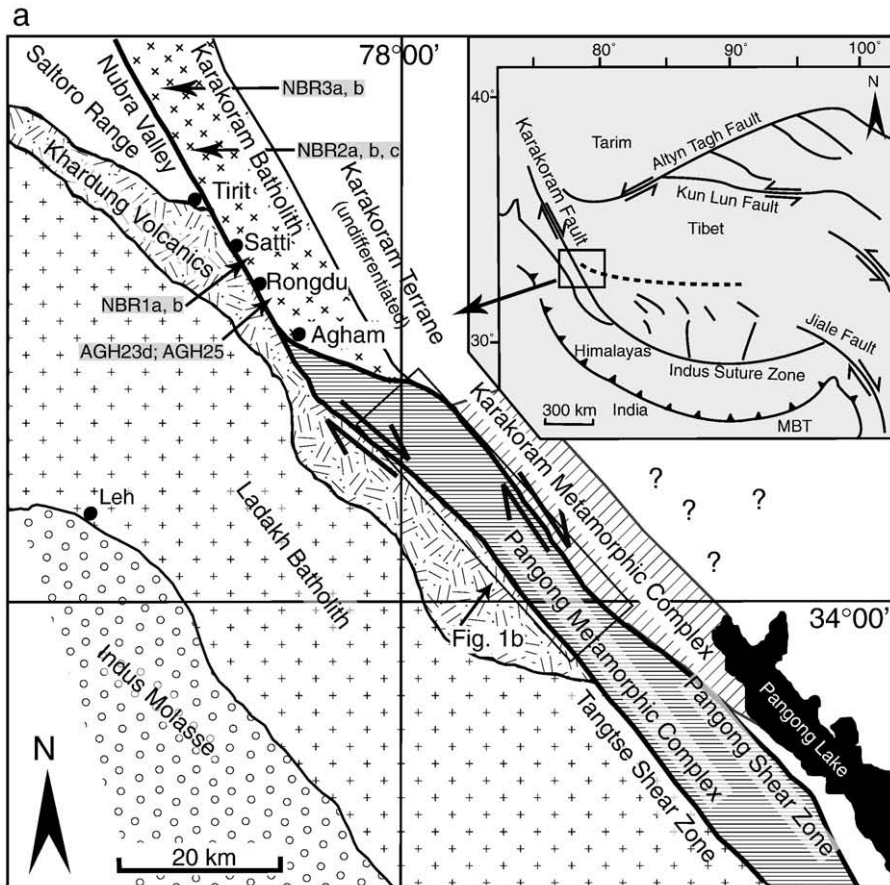
Granitic magma generation in continental collision zones can involve various source rocks and takes place under a range of conditions. Isotopic compositions of magmatic bodies are widely applied to trace their origin as the source rocks leave their isotopic fingerprint on the magmas (e.g. Beard et al., 2005). Granitoids with isotopic signatures intermediate between those of crustal and mantle sources, indicate that mixing of different magmas may have been involved (e.g. Andersson, 1991; Guillot and Le Fort, 1995; Hawkesworth and Vollmer, 1979). Generally, Himalayan Miocene leucogranites are examples of crustal melting with clear crustal isotopic signature (Deniel et al., 1987;

Le Fort et al., 1987; Guillot and Le Fort, 1995). Broadly contemporaneous leucogranites of the Karakoram Range in the western parts of the Himalayan orogen, however, have isotopic signatures intermediate between mantle and crust (Schärer et al., 1990; Searle et al., 1992; Crawford and Searle, 1992; Mahéo et al., 2002; Mahéo et al., 2009). The signature was explained by Mahéo et al. (2002) as resulting from break-off of the subducted Indian lithosphere causing higher heat flow from the asthenosphere and melting of metasomatised mantle of the Asian lithosphere. These melts then mixed with crustal melts. Mixing of magmas derived from a mantle and a crustal source has also been suggested by Crawford and Searle (1992) and Rex et al. (1988) who concluded that mantle-derived lamprophyre dykes found in the Karakoram could have influenced crustal magmas.

In the Tangtse–Shyok region of the Pangong Range within the Karakoram Shear Zone, in Ladakh, NW India (Fig. 1), migmatites are

\* Corresponding author.

E-mail address: [Henning.Reichardt@sci.monash.edu.au](mailto:Henning.Reichardt@sci.monash.edu.au) (H. Reichardt).



associated with leucogranite intrusions (Weinberg and Searle, 1998; Weinberg and Mark, 2008; Weinberg et al., 2009). Leucosomes are linked to leucogranites that form a complex intrusive sheet network linked to stocks and plutons that extend along the shear zone towards the Karakoram Batholith to the NW (Fig. 1a). In this paper, we present new geochemical, isotopic and geochronological data which support a link between magma migration and mixing processes that took place in the exposed migmatitic crustal source. This has led to the hybrid isotopic signature of the Karakoram Batholith. In the following, we introduce the Karakoram Shear Zone and describe the migmatites and their field relationships with leucogranite intrusions, including an overview of their geochemistry. Sr–Nd isotope and U–Pb SHRIMP results are then used to test field-based interpretations and to support regional-scale inferences.

## 2. Regional geology

The Karakoram Shear Zone lies in the central part of the Karakoram Fault and separates the Karakoram Terrane to the NE, from the Ladakh Terrane to the SW (Fig. 1a) (e.g. Raz and Honegger, 1989; Searle et al., 1998; Weinberg and Dunlap, 2000). The Karakoram Shear Zone itself is part of a crustal-scale, possibly lithospheric-scale (Lacassin et al., 2004; Rolland and Pêcher, 2001) strike–slip fault system that accommodates the northward push of the Indian plate into Eurasia and is characterized by dextral strike–slip motion, trending NW–SE, traceable for at least 700 km. The Karakoram Shear Zone in the Pangong Range area, in NE Ladakh is bounded by two roughly parallel mylonitic shear strands (Fig. 1a, b). The Tangtse Shear Zone (SW strand) dips 70° NE and separates the Pangong Metamorphic Complex (PMC) to the NE from the Ladakh Batholith to the SW. The Pangong Shear Zone (NE strand) is sub-vertical to steeply dipping SW, and separates the PMC from rocks of the Karakoram Terrane and the Karakoram Metamorphic Complex (KMC). The Karakoram Batholith crops out alongside the Nubra Valley to the NE of the Karakoram Shear Zone.

South of the PMC, the Ladakh Batholith granitoids comprise mainly Bt–Hbl granodiorites, commonly with mafic magmatic enclaves. The overlying Kardhung Volcanics are extrusive equivalents of the granitoids. This batholith is part of the Ladakh–Kohistan arc system with crystallization ages between 49 and 103 Ma (Honegger et al., 1982; Weinberg and Dunlap, 2000; Upadhyay et al., 2008; Ravikant et al., 2009). The PMC comprises a calc-alkaline granitoid suite, a meta-sedimentary rock sequence and leucogranite intrusions.

The calc-alkaline suite is dominated by a large body that we refer to as the Muglib Batholith. It is comprised mainly of Hbl–Bt–granodiorite, Bt–granodiorite and diorite. It extends at least from the area close to the Pangong Lake northwestwards to the Shyok Valley and links up discontinuously to the Tirit granite at the northeastern flanks of the Saltoro Range in the Nubra Valley further NW (Weinberg et al., 2000) through a number of dioritic–granodioritic bodies (Fig. 1a, b). The Muglib Batholith thus crops out for at least 85 km along strike of the Karakoram Shear Zone. The meta-sedimentary sequence comprises Bt–psammites, Bt–pelites, Bt–Hbl gneisses ranging to amphibolites and calc-silicate rocks. Minor beds of marble crop out in the Tangtse Shear Zone (Dunlap et al., 1998; Weinberg and Searle, 1998; Phillips et al., 2004). The calc-alkaline granitoids and meta-sedimentary sequence are migmatized, giving rise to leucogranite intrusions (Weinberg et al., 2009). Leucogranites, including pegmatitic dykes, are mostly two mica ± garnet leucogranites and Bt–leucogranites, and have crystallization ages between  $19.1 \pm 1.1$  Ma (Ravikant et al., 2009) and  $13.7 \pm 0.2$  Ma (Phillips et al., 2004).

The Karakoram Metamorphic Complex (KMC), NE of the Pangong Range consists mainly of pelitic Grt–St-bearing Bt–schists, amphibolites and marbles (Searle and Tirrul, 1991; Dunlap et al., 1998). The

Karakoram Batholith crops out along strike of the Pangong Range and of the Karakoram Shear Zone further NW in the Nubra Valley as a 6 to 7 km wide band (Fig. 1a; Searle et al., 1998; Weinberg et al., 2000).

Strain in the PMC is strongly partitioned into the main mylonitic shear strands and deformation intensity decreases away from these. Fold axes of isoclinal folds within the PMC plunge moderately (20–30°) towards NW (320–345°). A continuous schistosity is defined by aligned biotite and, when present, hornblende. It generally trends 320–330° and has a stretching lineation defined by biotite and stretched quartz grains plunging gently to moderately (generally 10–40°, rarely horizontal) towards NW in amphibolite facies rocks. Consistent dextral S–C–C' fabrics throughout the PMC indicate dextral transpressional shearing with a NE-side-up component (Searle et al., 1998). A greenschist facies overprint is locally evident along the mylonitic Pangong Shear Zone where Ms, Ep and Chl (mineral abbreviations after Kretz, 1983) stretching lineations plunge moderately SE, indicating fault reactivation with a NE-side-down component. Evidence for present-day movements in the area has been reported only in one locality from the Pangong Shear Zone, whereas the Tangtse Shear Zone seems to be inactive (Brown et al., 2002; Rutter et al., 2007). There are wide variations in the estimation of total offset and the current slip rate along the Karakoram Shear Zone (see Valli et al., 2007 for discussion). Estimates of recent movements are in the range of  $4 \pm 1$  mm/a (Brown et al., 2002),  $3.4 \pm 5$  mm/a (Jade et al., 2004) or as low as  $1 \pm 3$  mm/a (Wright et al., 2004).

## 3. Methodology

### 3.1. Geochemical analysis

For major element and trace element analysis, pulverized whole rock samples were analyzed after preparation of fused discs and pressed pellets, respectively, in a Bruker-AXS S4 Pioneer XRF Spectrometer at the Advanced Analytical Centre (AAC) of James Cook University. In Table 1 and appendix A, only samples labeled with \* were analyzed for trace elements by XRF. For all other samples, trace elements were analyzed using a Thermo Finnigan X series II, quadrupole ICP-MS. Sample solutions were produced from approximately 50 mg of sample powder using high pressure digestion methods. ICP-MS count rates were externally standardized by means of calibration curves based on the USGS standard reference material AGV-1 and RGM-1 following Eggins et al. (1997) for their trace element contents. Drift corrections were applied by the combined use of In, Bi as internal standards. Reproducibility on replicate analyses and accuracy was in the order of 5% for all elements.

### 3.2. Rb–Sr and Sm–Nd isotope geochemistry

Radiogenic isotope analytical work was carried out in the VIEPS facilities at the University of Melbourne, following procedures described in detail by Maas et al. (2005). The isotopic data were obtained with a NU Plasma multi-collector ICP-MS coupled to a CETAC Aridus desolvating nebulizer operated at an uptake rate of 40 µl/min. Typical sensitivity in this set-up is in the range of 100–130 V/ppm Sr or Nd. Instrumental mass bias was corrected by normalizing to  $^{88}\text{Sr}/^{86}\text{Sr} = 8.37521$  and  $^{146}\text{Nd}/^{145}\text{Nd} = 2.0719425$  (equivalent to  $^{146}\text{Nd}/^{144}\text{Nd} = 0.7219$ , Vance and Thirlwall, 2002), using the exponential law as part of an online iterative spike-stripping/internal normalization procedure. Data are reported relative to the accepted values for the standards: La Jolla  $^{143}\text{Nd}/^{144}\text{Nd} = 0.511860$  and SRM987  $^{86}\text{Sr}/^{87}\text{Sr} = 0.710230$ . This secondary normalization yields the following results for international standards ( $\pm 2\text{sd}$ ): BCR-1  $^{143}\text{Nd}/^{144}\text{Nd} = 0.512641 \pm 18$ , BHVO-1 =  $0.512998 \pm 18$ , JNdi-1 =  $0.512113 \pm 22$ ; and for  $^{86}\text{Sr}/^{87}\text{Sr}$  E&A Sr =  $0.708005 \pm 47$ , BCR-1 =  $0.705016 \pm 46$ , BHVO-1 =  $0.703478 \pm 36$ . These results

**Fig. 1.** (a) Geological sketch map of the Eastern Karakoram, based on Weinberg and Searle (1998). For explanations see text. Locations for samples from the Karakoram Batholith are shown. (b) Geological overview map of the Karakoram Shear Zone and sample locations.

**Table 1**  
Analysis of representative samples.

Type	Leucogranite Tangtse Pluton				<i>In situ</i> leucosome		Hbl-bearing leucosome		Leucogranite Dyke	
Sample	TNG166	TNG71a*	TNG167a	TNG161a	TNG170	TNG171	TNG60d	AGH23a	TNG174b	TNG186
Coordinates	34°04'10.5"N 78°13'39.4"E	34°03'42.6"N 78°13'52.2"E	34°03'57.7"N 78°13'37.2"E	34°02'35.6"N 78°13'16.0"E	34°02'50.1"N 78°13'02.7"E	34°03'25.3"N 78°14'13.3"E	34°25'10.6"N 77°49'23.5"E	34°01'26.7"N 78°12'12.9"E	34°08'41.8"N 78°08'17.8"E	
Major elements wt.%										
SiO <sub>2</sub>	70.83	73.40	74.10	73.55	72.09	75.53	62.3	58.1	72.11	71.16
TiO <sub>2</sub>	0.29	0.09	0.17	0.06	0.13	0.06	0.57	0.70	0.19	0.22
Al <sub>2</sub> O <sub>3</sub>	15.55	14.90	15.33	14.89	15.96	14.72	16.3	12.5	16.24	15.41
Fe <sub>2</sub> O <sub>3t</sub>	1.57	0.63	0.93	0.59	0.71	0.39	2.30	4.61	1.15	1.37
MnO	0.03	0.02	0.01	0.02	0.01	0.01	0.06	0.13	0.01	0.02
MgO	0.33	bd	0.26	0.26	0.26	0.26	1.31	3.88	0.48	0.40
CaO	1.79	1.71	1.97	1.73	2.37	2.37	2.65	8.05	3.99	2.09
Na <sub>2</sub> O	4.02	3.73	3.66	3.90	4.33	3.57	1.68	1.92	3.68	3.28
K <sub>2</sub> O	4.50	4.76	4.15	3.76	2.98	2.94	10.1	6.53	1.69	4.56
P <sub>2</sub> O <sub>5</sub>	0.09	0.02	0.03	0.01	0.03	0.02	0.40	2.06	0.07	0.09
LOI	0.46	0.77	0.39	0.33	0.47	0.34	0.46	0.59	0.41	0.44
Total	99.45	99.95	101.00	99.07	99.34	100.20	98.1	99.0	99.99	99.04
A/CNK	1.06	1.03	1.09	1.09	1.09	1.10	0.88	0.50	1.07	1.09
Mg/(Fe <sup>+</sup> Mg)	0.29	0.00	0.36	0.47	0.42	0.57	0.53	0.63	0.45	0.37
Trace elements ppm										
Sc	1.3	bd	1.2	0.6	0.5	0.3	6.1	16.4	1.0	2.0
Ba	1963.1	849	641.2	80.4	1360.1	1320.4	8279.9	4136.1	533.3	1500.7
Ti	973.8	593	687.9	112.5	553.2	185.8	2551.2	4068.8	830.5	966.2
V	14.0	7	6.9	bd	9.1	2.9	38.0	75.4	10.9	15.7
Cr	bd	23	bd	bd	1.7	0.3	36.6	60.9	0.9	0.7
Mn	153.4	69	97.5	52.1	41.4	39.4	348.7	928.0	67.4	125.2
Co	38.5	1	55.9	26.2	68.6	79.4	20.3	35.1	67.6	46.7
Ni	0.9	4	0.3	-0.6	3.1	1.0	28.2	39.2	1.4	1.3
Cu	7.6	14	0.4	0.2	39.7	7.8	31.6	66.0	2.6	3.4
Zn	29.5	24	27.1	18.5	8.4	6.1	38.7	86.1	28.8	26.9
Ga	23.2	16	13.2	4.0	20.0	21.8	165.3	13.9	12.3	21.5
Pb	86.6	55	55.5	62.2	15.7	14.2	85.4	30.2	24.7	34.1
Rb	321.0	156	172.8	176.4	52.1	57.4	440.9	151.4	80.4	140.6
Sr	741.1	398	433.1	162.1	1090.0	816.2	1083.2	903.4	542.5	438.8
Y	5.3	2	2.3	2.1	1.0	1.4	20.9	29.9	3.2	3.9
Zr	54.9	39	18.4	14.3	6.5	6.6	39.7	30.4	8.4	23.0
Nb	7.8	4	2.8	7.2	1.3	0.5	9.7	21.2	2.4	4.2
Th	58.6	bd	4.1	0.6	0.8	2.2	93.3	21.3	27.3	27.0
U	8.4	bd	1.0	0.6	0.1	0.2	6.5	3.7	0.8	1.0
Rb/Sr	0.43	0.39	0.40	1.09	0.05	0.07	0.41	0.17	0.15	0.32

compare well with data based on TIMS from other laboratories (e.g. Maas and McCulloch, 1991; Tanaka et al., 2000; Raczek et al, 2003). Typical within-run precisions (2se) are  $\pm 0.000010$  ( $^{143}\text{Nd}/^{144}\text{Nd}$ ) and  $\leq \pm 0.000020$  ( $^{86}\text{Sr}/^{87}\text{Sr}$ ), while external precision (reproducibility, 2sd) based on the results for secondary standards is  $\pm 0.000020$  (Nd) and  $\pm 0.000040$  (Sr). External precision for  $^{87}\text{Rb}/^{86}\text{Sr}$  and  $^{147}\text{Sm}/^{144}\text{Nd}$  obtained by isotope dilution is  $\pm 0.5\%$  and  $\pm 0.2\%$ , respectively. Parent/daughter ratios obtained by Q-ICP-MS (Monash University) for unspiked samples have uncertainties of  $\pm 2\%$  to  $\pm 3\%$  for  $^{87}\text{Rb}/^{86}\text{Sr}$  and  $\pm 3\%$  to  $\pm 5\%$  for  $^{147}\text{Sm}/^{144}\text{Nd}$ , respectively.

The Sm–Nd and Rb–Sr analytical work of the samples from the Ladakh Batholith (marked with \*\* in Table 5) were performed at the Laboratory for Isotope Geology at the Swedish Museum of Natural History and followed the analytical procedure reported in Andersson et al. (2002). The average of measurements of the Lajolla Nd standard during the measurements of samples LEH40 and LEH52 was  $0.511843 \pm 13$  (1 s, n=13), and during measurements of the other samples  $0.511844 \pm 5$  (1 s, n=10). No correction was applied. Similarly, an average of the measurements of the SRM987 Sr standard during measurements of the samples was  $0.710245 \pm 32$  (1 s, n=16). No correction was applied.

Age corrections (18–100 Ma) for the samples analyzed here are generally small, amounting to  $< 1$  unit for  $\epsilon_{\text{Nd}}$  and  $\sim 0.00100$  (mostly much less) for  $^{87}\text{Sr}/^{86}\text{Sr}$ . The propagated error for initial  $\epsilon_{\text{Nd}}$  is  $\sim \pm 0.5$

unit and 0.00007 or less for initial  $^{87}\text{Sr}/^{86}\text{Sr}$ . Propagated errors for samples analyzed unspiked (i.e. with Rb/Sr and Sm/Nd by Q-ICP-MS) are similar. The decay constants used are:  $^{87}\text{Rb}$   $1.42 \cdot 10^{-11}/\text{yr}$ ;  $^{147}\text{Sm}$   $6.54 \cdot 10^{-12}/\text{yr}$ .

### 3.3. U–Pb SHRIMP analysis

Zircon and titanite grains were separated from whole rock samples using standard crushing, washing, heavy liquid (density 2.96 and 3.3), and paramagnetic procedures. The zircon and titanite concentrates were hand picked and placed onto double-sided tape, mounted in epoxy together with chips of the reference zircons (Temora, and SL13) and titanite (BLR-1), sectioned approximately in half, and polished. Sample TNG148b was analyzed *in situ* in a polished thin section. Reflected and transmitted light photomicrographs were obtained for all zircons. Cathodoluminescence (CL) and Scanning Electron Microscope (SEM) images were prepared for all zircon grains; back scattered SEM (BSE) images were prepared for the titanite grains. These CL and BSE images were used to decipher the internal structures of the sectioned grains and to ensure that the  $\sim 20 \mu\text{m}$  SHRIMP spot was wholly within a single age component within the sectioned grains.

The U–Th–Pb analyses were made using the SHRIMP II at the Research School of Earth Sciences, The Australian National University, Canberra, Australia, following procedures given in Williams (1998,

Pegmatite Dyke			Leucogranite Shyok Valley			Karakoram Batholith				
TNG187a	TNG187b	TNG187c	TNG195	TNG196	TNG197e	Leucogranite				
	34°08'48.6"N		34°18'06.8"N	34°18'07.2"N	34°17'39.6"N	AGH25a	NBR1b	NBR2a	NBR3b	
	78°08'26.9"E		78°00'46.2"E	78°00'46.6"E	78°02'02.9"E	34°27'04.4"N	34°29'06.0"N	34°37'54.6"N	34°46'27.5"N	
						77°45'53.1"E	77°44'20.0"E	77°38'24.1"E	77°32'45.7"E	
Major elements wt.%										
75.12	74.35	75.41	70.79	73.31	71.91	72.3	73.40	72.92	73.83	
0.05	0.05	0.07	0.32	0.17	0.22	0.27	0.22	0.24	0.20	
14.14	14.01	14.21	15.40	14.92	15.61	14.9	14.89	14.92	14.07	
0.74	1.04	0.72	1.70	0.98	1.17	1.88	1.42	1.51	1.39	
0.05	0.06	0.03	0.04	0.02	0.02	0.03	0.02	0.04	0.03	
0.26	0.26	0.26	0.45	0.26	0.27	0.43	0.29	0.28	0.26	
1.52	1.38	1.65	2.19	1.65	2.17	2.61	1.60	1.77	1.68	
4.11	3.54	3.85	3.87	3.91	4.15	4.03	3.79	3.80	3.18	
3.30	4.36	3.73	3.77	4.27	3.66	2.26	3.64	3.65	4.11	
bd	0.01	bd	0.10	0.04	0.05	0.07	0.06	0.09	0.07	
0.21	0.22	0.49	0.47	0.37	0.35	0.80	0.64	0.86	0.80	
99.47	99.25	100.41	99.07	99.88	99.58	99.6	99.95	100.07	99.60	
1.08	1.07	1.06	1.07	1.06	1.06	1.08	1.14	1.11	1.10	
0.41	0.33	0.42	0.34	0.34	0.31	0.31	0.29	0.27	0.27	
Trace elements ppm										
2.6	2.3	1.2	1.1	1.1	1.7	2.1	1.8	8.0	1.9	
21.8	51.8	93.2	1404.6	893.4	997.1	860.2	679.2	1000.5	789.8	
182.7	151.4	206.1	990.9	665.7	903.2	688.3	742.8	3946.8	723.3	
3.2	5.3	1.9	16.1	11.7	14.6	4.5	10.9	76.2	6.5	
bd	bd	bd	bd	bd	0.1	55.2	bd	9.9	bd	
382.0	387.0	170.3	188.8	114.3	130.0	144.3	132.7	476.3	160.4	
65.5	60.7	67.1	27.4	44.0	37.5	69.3	0.9	8.1	0.9	
0.1	0.0	0.6	1.6	1.0	1.3	1.0	bd	12.3	bd	
6.0	2.4	1.8	2.1	6.0	9.1	2.7	0.9	36.1	bd	
12.3	13.4	9.5	29.6	21.1	26.6	17.8	20.0	48.2	26.5	
4.7	4.3	4.6	17.8	16.8	17.0	14.4	11.9	17.5	13.4	
50.9	49.5	40.7	69.7	89.0	60.1	52.3	35.7	37.4	40.5	
145.8	162.1	131.2	140.6	219.4	164.1	161.5	201.1	208.7	201.3	
66.3	78.4	121.2	546.2	563.5	597.5	146.8	363.2	501.3	336.8	
15.7	16.7	6.3	5.2	2.2	3.5	8.6	6.2	13.8	10.1	
27.7	63.9	10.2	27.8	29.5	48.6	31.5	30.8	95.2	41.6	
2.6	2.9	1.9	6.3	3.2	4.7	8.5	6.4	12.5	8.5	
4.0	7.3	1.2	40.4	31.6	27.5	15.8	15.6	20.0	20.2	
2.0	1.9	0.5	4.0	6.9	2.5	4.2	1.4	4.9	3.5	
2.20	2.07	1.08	0.26	0.39	0.27	1.1	0.55	0.42	0.60	

(continued on next page)

and references therein). Each analysis consisted of 6 scans through the mass range, with a U–Pb reference grain analyzed for every three unknown analyses. The data have been reduced using the SQUID Excel Macro of Ludwig (2001).

For the zircon analyses, the U/Pb ratios have been normalized relative to a value of 0.0668 for the Temora reference zircon, equivalent to an age of 417 Ma (see Black et al., 2003). Uncertainties in the U–Pb calibration were 0.40% for TNG62a and TNG131a analytical sessions, and 1.18% for *in situ* analysis of TNG148b. The U–Pb ratios for titanite were normalized relative to the BLR-1 standard (1051 Ma, Aleinikoff et al., 2007). Uncertainties in the U–Pb calibrations were 0.43% for titanite SHRIMP sessions TNG131a and TNG148a.

Uncertainties given for individual analyses (ratios and ages) are at the one sigma level (Tables 2–4). Tera and Wasserburg (1972) concordia plots, probability density plots with stacked histograms and weighted mean  $^{206}\text{Pb}/^{238}\text{U}$  age calculations were carried out using ISOPLOT/EX (Ludwig, 2003).

#### 4. Field relations and anatexis in the Tangtse and Darbuk–Shyok areas

The Tangtse and Darbuk–Shyok gorges are cut by the Tangtse River roughly perpendicular to strike of the Karakoram Shear Zone, 20 km apart. Here, a mid-crustal section including the main lithologies of the PMC is exposed between the Tangtse Shear Zone and the Pangong

Shear Zone (Fig. 2a). These migmatized rocks will be described here following the terminology suggested by Sawyer (2008).

##### 4.1. Meta-sedimentary sequence

This sequence comprises Bt–psammmites, Bt–pelites, Bt–Hbl gneisses ranging to amphibolites, and calc-silicate rocks. These rock types are interlayered at the scale of tens of meters to hundreds of meters. Bt–psammmites and Bt–pelites are generally characterized by the mineral assemblage Bt + Pl + Qtz ± Grt, and muscovite occurs in retrograde shear zones. Common accessory phases are Ap + Ttn + Mag + Mnz + Aln + Zrn. We found sillimanite in only one sample of PMC meta-sedimentary rocks, but its occurrence has also been reported by Rolland and Pêcher (2001). Calc-silicate rocks generally contain Cpx + Hbl + Pl + Qtz ± Bt ± Cc.

Whilst calc-silicate rocks and mafic amphibolites ( $\text{SiO}_2 < 50 \text{ wt } \%$ ) do not present evidence for anatexis, Bt–psammmites and Bt-bearing amphibolites have leucosomes that are interpreted to be the remainders of crystallized melt that segregated from the melanosome. Diffuse leucosome patches are common, and layer-parallel leucosomes in stromatic migmatites have melanosome rims that consist mostly of biotite. Leucosomes in migmatitic Bt–psammmites range in composition from leucotonalite to leucogranite and commonly contain garnet. Leucosomes in the Hbl-rich gneissic to amphibolitic

Table 1 (continued)

Type	Muglib Batholith					Pangong Metamorphic Complex			
	Granodiorite		Diorite		Gabbro	Bt-psammite		Amphibolite	Calc-silicate
Sample	TNG131a*	TNG207	TNG169a	TNG205a	AGH5	TNG131d*	TNG167b	TNG108c*	TNG208
Coordinates	34°03'38.8"N	34°03'01.4"N	34°02'40.3"N	34°02'38.3"N	34°18'47.7"N	34°03'38.8"N	34°03'40.4"N	34°08'42.0"N	34°01'33.5"N
	78°13'52.1"E	78°13'41.3"E	78°13'07.8"E	78°13'25.4"E	77°52'03.8"E	78°13'52.1"E	78°13'52.7"E	78°08'18.5"E	78°12'01.7"E
Major elements wt.%									
SiO <sub>2</sub>	67.50	68.23	61.95	54.91	52.4	61.60	60.99	52.82	52.49
TiO <sub>2</sub>	0.56	0.50	0.70	1.37	1.10	0.83	0.82	1.01	0.64
Al <sub>2</sub> O <sub>3</sub>	16.30	15.26	14.29	17.56	19.8	17.00	16.97	15.55	14.69
Fe <sub>2</sub> O <sub>3t</sub>	3.49	3.05	5.18	8.04	7.91	6.56	6.85	8.94	5.77
MnO	0.09	0.07	0.15	0.13	0.15	0.11	0.10	0.15	0.11
MgO	1.57	1.22	4.55	3.01	2.93	2.84	3.27	7.18	3.74
CaO	3.16	2.85	6.46	5.90	7.89	5.23	3.77	10.03	15.00
Na <sub>2</sub> O	4.37	3.17	3.01	3.81	3.22	1.82	2.00	3.47	0.98
K <sub>2</sub> O	2.85	4.57	2.47	2.97	1.04	3.02	3.25	0.73	3.41
P <sub>2</sub> O <sub>5</sub>	0.22	0.19	0.14	0.50	0.27	0.16	0.15	0.09	0.15
LOI	0.50	0.57	0.93	0.82	2.92	1.06	1.59	0.36	2.03
Total	100.62	99.65	99.83	99.00	99.6	100.17	99.74	100.30	98.99
A/CNK	1.02	0.99	0.74	0.87	0.95	1.08	1.24	0.63	0.45
Mg/(Fe <sup>+</sup> Mg)	0.47	0.44	0.64	0.43	0.42	0.46	0.49	0.61	0.56
Trace elements ppm									
Sc	9	5.4	19.9	12.7	17.5	22	11.5	37	16.2
Ba	337	379.7	586.5	540.1	154.0	448	255.1	19	396.5
Ti	4103	2121.4	3833.4	7373.2	5423.7	7362	3270.7	5844	3419.7
V	87	49.7	103.7	123.5	193.0	186	95.1	235	119.0
Cr	63	21.1	74.8	12.7	20.9	178	124.8	220	102.9
Mn	790	415.1	1053.4	859.2	910.1	909	497.3	1183	737.8
Co	7	36.2	45.1	27.6	18.5	20	43.4	47	22.7
Ni	32	13.4	53.5	16.7	7.2	62	76.5	57	48.9
Cu	17	6.3	21.5	47.7	23.2	24	20.1	84	12.8
Zn	81	38.4	62.6	86.7	73.3	112	72.1	61	73.2
Ga	20	8.9	12.6	14.4	17.6	20	6.5	15	9.4
Pb	43	20.5	12.4	12.2	5.0	29	20.7	8	25.5
Rb	199	161.1	49.4	124.1	26.5	168	253.5	10	153.9
Sr	379	413.3	547.6	568.6	497.3	159	96.6	132	339.7
Y	19.00	17.6	18.8	24.3	20.2	28	20.7	25	22.4
Zr	164	18.8	11.5	58.6	7.9	185	6.7	86	11.2
Nb	27	15.0	18.2	25.5	5.7	25	12.8	9	11.1
Th	15	15.2	1.1	11.2	1.8	12	12.9	2	10.6
U	bd	2.2	2.1	1.1	0.3	bd	2.1	bd	1.8
Rb/Sr	0.53	0.39	0.09	0.22	0.05	1.06	2.62	0.08	0.45

rocks of this sequence commonly contain large poikilitic hornblende crystals (Fig. 3a).

In the central part of the Tangtse gorge there are metatexites and diatexites (indicated in cross section, Fig. 2a) that have melanosomes ranging compositionally from Hbl–Bt–schists to amphibolitic gneisses. Leucosomes in these rocks are Bt–leucogranites, Hbl–Bt–leucogranites and leucotonalites. Interplay between folding, shearing and magma migration in these meta- and diatexites has been described by Weinberg and Mark (2008). Typically, layer-parallel leucosomes in metatexites are linked with leucosomes parallel to the axial plane in folds. Folded leucosomes also cut through fold limbs and connect to leucosomes of different layers (Fig. 4). Fold hinges are truncated by axial planar shearing which further facilitates leucosome interconnection. Disruption of melanosomes, especially in the diatexites leads to a large range of compositions and a heterogeneous rock where distinction between leucosome and melanosome is blurred. In either meta- or diatexite the exact nature of the protolith is obscured by compositional changes related to melt extraction.

#### 4.2. Calc-alkaline granitoids

The main facies of the Muglib Batholith is a medium to coarse-grained titanite bearing Hbl–Bt–granodiorite, commonly with Ap + Aln + Zrn as accessory minerals and decimetric mafic magmatic enclaves. A continuous foliation is defined by aligned Hbl, Bt and Ttn grains. Within the main facies, there are up to 100 m long lenses of Hbl–Cpx diorite. A Bt–

granodiorite occurs at the margins of the batholith and forms a border facies which crops out close to the Pangong Shear Zone near Muglib Village (Fig. 1b), and also intrudes the meta-sedimentary country rocks as dykes.

Migmatization of the Muglib Batholith is evident in the Bt–granodiorite border facies, in patches of the main facies as well as in the Hbl–Cpx diorite lenses. Leucosomes parallel to the dominant foliation parallel to the Karakoram Shear Zone are continuous with crosscutting leucosomes, thus forming a network interpreted to represent a melt flow network during anatexis (Weinberg and Searle, 1998). Melanosome rims are generally present and consist of mostly biotite and hornblende around leucosomes. Up to 3 cm large euhedral poikilitic hornblende crystals in leucosomes are common especially in diorites but rare in the Hbl-free border facies. In these migmatitic diorites, leucosomes that dominantly consist of Hbl megacrysts and Kfs (Fig. 3b) are interpreted as a residual assemblage after the melt was extracted.

#### 4.3. Leucogranites

Leucogranites are ubiquitous in the Karakoram Shear Zone either as dykes, stocks on the scale of tens to hundreds of meters or kilometer-sized plutons (Fig. 1b, 2) such as the Darbuk Pluton, a sheared Ms–Bt ± Grt–leucogranite (Fig. 1b) or the Tangtse Pluton which is related to the Pangong Injection Complex that is depicted in Fig. 2b (Weinberg and Searle, 1998; Weinberg et al., 2009). The

**Table 2**  
U–Pb SHRIMP data; sample TNG62a.

Zircon analysis																
Coordinates		34°02'16.8"N														
		78°14'57.7"E														
Grain. spot	U (ppm)	Th (ppm)	Th/U	<sup>206</sup> Pb*	<sup>204</sup> Pb/ <sup>206</sup> Pb	±	f <sub>206</sub> %	<sup>238</sup> U/ <sup>206</sup> Pb	±	<sup>207</sup> Pb/ <sup>206</sup> Pb	±	<sup>206</sup> Pb/ <sup>238</sup> U	±	Radiogenic age (Ma)	<sup>206</sup> Pb/ <sup>238</sup> U	±
1.1	924	516	0.56	7.6	0.000084	–	0.05	104.82	1.19	0.0477	0.0009	0.0095	0.0001	61.2	0.7	
1.2	358	277	0.78	3.5	–	–	0.23	88.01	1.12	0.0493	0.0014	0.0113	0.0001	72.7	0.9	
2.1	2137	1398	0.65	20.9	0.000093	–	<0.01	87.73	1.11	0.0473	0.0008	0.0114	0.0001	73.1	0.9	
2.2	421	317	0.75	4.0	–	–	0.14	91.00	1.16	0.0485	0.0014	0.0110	0.0001	70.4	0.9	
3.1	136	100	0.74	1.2	0.001987	–	0.31	93.94	1.38	0.0498	0.0024	0.0106	0.0002	68.1	1.0	
4.1	403	294	0.73	3.9	0.000515	–	0.04	89.54	1.15	0.0478	0.0014	0.0112	0.0001	71.6	0.9	
5.1	185	118	0.64	1.8	0.000872	–	0.40	89.50	1.37	0.0506	0.0020	0.0111	0.0002	71.3	1.1	
6.1	123	109	0.89	1.1	0.000938	–	0.39	93.46	1.68	0.0505	0.0027	0.0107	0.0002	68.3	1.2	
7.1	227	159	0.70	2.2	0.000981	–	0.62	90.68	1.33	0.0523	0.0019	0.0110	0.0002	70.3	1.0	
8.1	229	252	1.10	2.2	0.000518	–	0.26	88.05	1.29	0.0495	0.0018	0.0113	0.0002	72.6	1.1	
9.1	385	273	0.71	3.8	–	–	0.75	88.10	1.14	0.0534	0.0032	0.0113	0.0002	72.2	1.0	
10.1	171	163	0.95	1.7	0.001165	–	<0.01	86.10	1.50	0.0466	0.0021	0.0116	0.0002	74.5	1.3	
11.1	239	163	0.68	2.3	0.000502	–	0.27	90.65	1.38	0.0495	0.0018	0.0110	0.0002	70.5	1.1	
11.2	2525	1941	0.77	24.5	–	–	0.01	88.56	0.93	0.0475	0.0005	0.0113	0.0001	72.4	0.8	
12.1	298	226	0.76	2.8	0.001338	–	0.22	90.01	1.23	0.0491	0.0016	0.0111	0.0002	71.1	1.0	
12.2	1458	909	0.62	13.2	–	–	<0.01	94.82	1.04	0.0473	0.0008	0.0105	0.0001	67.6	0.7	
13.1	365	355	0.97	3.4	–	–	0.01	91.69	1.22	0.0475	0.0015	0.0109	0.0001	69.9	0.9	
13.2	1157	742	0.64	11.0	0.000018	–	0.01	90.01	1.00	0.0475	0.0008	0.0111	0.0001	71.2	0.8	
14.1	278	421	1.52	2.7	–	–	0.03	89.34	1.26	0.0477	0.0017	0.0112	0.0002	71.7	1.0	
15.1	470	331	0.70	4.4	0.000711	–	0.47	91.03	1.14	0.0511	0.0013	0.0109	0.0001	70.1	0.9	
16.1	526	286	0.54	5.0	0.000199	–	0.08	90.25	1.52	0.0481	0.0012	0.0111	0.0002	71.0	1.2	
16.2	390	324	0.83	3.7	–	–	0.27	90.49	1.17	0.0496	0.0014	0.0110	0.0001	70.7	0.9	
17.1	677	612	0.90	6.6	0.000189	–	0.19	88.15	1.03	0.0490	0.0018	0.0113	0.0001	72.6	0.9	

f<sub>206</sub> % denotes the percentage of <sup>206</sup>Pb that is common Pb.

Tangtse Pluton is approximately 1.3 km in length, has an outcrop height of ~600 m (Fig. 2b), and is a result of the amalgamation of multiple magma sheets that intruded Bt-psammites and which are still preserved as screens inside the pluton. Leucogranite sheets in the Pangong Injection Complex are most likely derived from a combination of local and intrusive magma sheets (Weinberg and Searle 1998, Weinberg et al., 2009). The pluton is petrographically heterogeneous consisting mainly of medium-grained Bt–leucogranite, Ms–Bt ± Grt leucogranite and coarse-grained Grt–Ms–leucogranite. Accessory minerals are commonly Ap, Zrn, Mnz, Aln and Grt. Only rarely, small and strongly corroded hornblende crystals are found.

The leucogranites are generally deformed and show S–C fabrics, and in some biotite-rich examples Bt-foliae that wrap around feldspar crystals or form asymmetric tails thereby defining dextral S–C–C' fabrics. In some cases, deformation fabrics are not apparent in hand specimen, because micas are lacking, but are visible under the microscope. Microstructures, however, reveal dextral S–C fabrics.

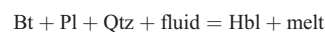
#### 4.4. Syndeformational melting

Leucosomes in shear bands suggest that these are either the loci of incipient partial melting or that melt migrated into and accumulated in these zones (Fig. 5). Like this structure, a number of field relationships between melt, faults, shear zones and folds have been interpreted to result from synkinematic melting (Weinberg and Mark, 2008). A common feature found in many of the least deformed leucogranite sheets is shown in Fig. 6 where a broad dextral S–C fabric is defined by the alignment of feldspar lozenges. The interstitial finer-grained Qtz and Pl are only weakly deformed and are interpreted as having crystallized directly from a melt, indicating synkinematic magma crystallization. We therefore take the view here that anatexis was contemporaneous with deformation. This was also the interpretation by Rolland et al. (2009) based on microstructural relationships, and contradicts the pre-kinematic view presented by Phillips et al. (2004).

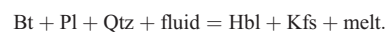
Deformation outlasted magmatism, continuing as the rock mass cooled to temperatures below 250 °C, as documented in microstructures in the Muglib area (Rutter et al., 2007) and Shiquanhe area further SE in the Karakoram Shear Zone (Valli et al., 2007). This low temperature deformation is reflected by porphyroclasts of K-feldspar and plagioclase in leucogranites with rims of fine-grained, sheared and recrystallized Kfs + Pl + Qtz (Fig. 6).

#### 4.5. Water-fluxed melting

The presence of large, poikilitic hornblende crystals in leucosomes in calc-alkaline granodiorites and diorites (Fig. 3, 6) and the lack of other obvious peritectic minerals, suggests melting in the presence of a H<sub>2</sub>O-rich fluid phase (Lappin and Hollister, 1980; Kenah and Hollister, 1983; Mogk, 1992). This interpretation is also supported by the lack of peritectic minerals in leucosomes in Bt–psammites (Weinberg and Mark, 2008). Mogk (1992) stressed the importance of water infiltration in order to form Hbl-bearing leucosomes in migmatites and proposed that shear zones form pathways for H<sub>2</sub>O-rich fluids. Accordingly, in the melting experiments of Gardien et al. (2000) hornblende was found as a crystallizing phase only when water was added. We suggest that the melting reactions proposed by McLellan (1988) and Lappin and Hollister (1980) account for hornblende-bearing leucosomes at calculated temperatures between 675 and 750 °C and 6 to 8 kbar,



or



Based on mineral paragenesis and thermobarometry, Rolland and Pêcher (2001) proposed that peak metamorphic temperatures in the Tangtse area reached 700 ± 20 °C at 7 ± 1 kbar, i.e. just below the onset of muscovite dehydration melting and well below



**Table 3**  
U–Pb SHRIMP data; sample TNG131a.

Zircon analysis														
Sample	TNG131a													
Coordinates	34°03'38.8"N 78°13'52.1"E													
Grain. spot	U (ppm)	Th (ppm)	Th/U	<sup>206</sup> Pb* (ppm)	<sup>204</sup> Pb/ <sup>206</sup> Pb	±	f <sub>206</sub> %	<sup>238</sup> U/ <sup>206</sup> Pb	±	<sup>207</sup> Pb/ <sup>206</sup> Pb	±	<sup>206</sup> Pb/ <sup>238</sup> U	±	Radiogenic age (Ma)
1.1	1696	1160	0.68	15.3	0.000129	-	<0.01	95.31	1.06	0.0472	0.0007	0.0105	0.0001	67.3
1.2	465	349	0.75	4.3	0.000176	-	0.28	92.15	1.15	0.0496	0.0013	0.0108	0.0001	69.4
2.1	553	551	1.00	5.2	0.000033	-	<0.01	90.87	1.19	0.0469	0.0012	0.0110	0.0001	70.6
2.2	258	184	0.71	2.4	0.000764	-	0.01	90.89	1.28	0.0475	0.0017	0.0110	0.0002	70.6
3.1	412	333	0.81	4.0	0.000571	-	0.34	88.57	1.12	0.0502	0.0013	0.0113	0.0001	72.1
4.1	134	185	1.38	1.2	-	-	0.28	92.72	1.61	0.0496	0.0025	0.0108	0.0002	69.0
5.1	643	600	0.93	6.3	0.000494	-	0.23	87.96	1.04	0.0493	0.0011	0.0113	0.0001	72.7
6.1	4364	4115	0.94	43.1	-	-	<0.01	87.01	0.90	0.0474	0.0004	0.0115	0.0001	73.7
7.1	54	55	1.01	0.5	0.003931	-	1.32	87.83	2.08	0.0580	0.0039	0.0112	0.0003	72.0
8.1	554	425	0.77	5.2	0.000254	-	0.33	91.85	1.12	0.0500	0.0012	0.0109	0.0001	69.6
9.1	451	333	0.74	4.2	0.000383	-	<0.01	91.89	1.16	0.0468	0.0013	0.0109	0.0001	69.8
9.2	303	139	0.46	2.9	-	-	0.17	88.97	1.21	0.0488	0.0015	0.0112	0.0002	71.9
10.1	325	202	0.62	3.1	0.001032	-	1.59	90.45	1.22	0.0600	0.0017	0.0109	0.0001	69.8
10.2	516	301	0.58	5.0	0.000040	-	0.20	87.88	1.07	0.0490	0.0012	0.0114	0.0001	72.8
11.1	251	244	0.97	2.5	0.000403	-	0.02	87.42	1.24	0.0477	0.0017	0.0114	0.0002	73.3
12.1	262	166	0.63	2.5	0.000520	-	0.27	90.75	1.28	0.0496	0.0017	0.0110	0.0002	70.5
12.2	250	170	0.68	2.3	0.000106	-	0.15	94.03	1.35	0.0486	0.0016	0.0106	0.0002	68.1
13.1	418	227	0.54	3.8	0.000424	-	0.32	93.91	1.20	0.0499	0.0014	0.0106	0.0001	68.1
14.1	506	433	0.86	4.9	-	-	0.03	89.51	1.09	0.0477	0.0012	0.0112	0.0001	71.6
15.1	113	175	1.55	1.1	-	-	<0.01	90.61	1.66	0.0466	0.0027	0.0110	0.0002	70.8
16.1	3055	2050	0.67	30.0	0.000070	-	0.08	87.39	0.91	0.0481	0.0005	0.0114	0.0001	73.3
17.1	196	106	0.54	1.8	0.001090	-	0.14	91.30	1.40	0.0486	0.0020	0.0109	0.0002	70.1
Zircon included in titanite														
2.1	593	273	0.46	6.8	0.013439	-	26.44	74.46	0.93	0.2569	0.0316	0.0099	0.0006	63.4
<b>Titanite analysis</b>														
1.1	406	48	0.12	1.7	0.031001	0.002476	57.9	202.99	2.87	0.4805	0.0064	0.0021	0.0003	13.4
2.1	146	29	0.20	0.9	0.028931	0.002446	54.0	141.04	2.41	0.4690	0.0084	0.0033	0.0004	21.0
3.1	180	7	0.04	0.9	0.034459	0.002420	64.4	167.62	2.71	0.4928	0.0081	0.0021	0.0003	13.7
3.2	37	396	10.61	0.6	0.021536	0.002722	40.0	55.11	1.34	0.4282	0.0096	0.0109	0.0010	69.8
4.1	98	6	0.06	0.7	0.034500	0.002938	64.4	116.85	2.20	0.6005	0.0110	0.0030	0.0006	19.6
5.1	107	71	0.67	0.8	0.035582	0.002774	66.4	108.33	1.98	0.5921	0.0107	0.0031	0.0006	20.0
5.2	34	456	13.49	0.6	0.027273	0.002768	50.7	45.15	1.11	0.4566	0.0096	0.0109	0.0013	70.0
6.1	88	65	0.73	1.0	0.020407	0.001886	38.0	72.92	1.31	0.3152	0.0085	0.0085	0.0006	54.6
7.1	64	466	7.30	1.0	0.030482	0.002392	56.7	57.19	1.13	0.5689	0.0092	0.0076	0.0010	48.6
7.2	91	27	0.30	0.8	0.031392	0.002969	58.6	101.37	2.01	0.5523	0.0107	0.0041	0.0006	26.3
8.1	99	369	3.73	1.1	0.013155	0.001402	24.5	74.71	1.30	0.2358	0.0046	0.0101	0.0004	64.8
8.2	54	671	12.47	0.9	0.029445	0.002516	54.8	53.98	1.16	0.5018	0.0092	0.0084	0.0010	53.8
6.2	57	435	7.62	0.7	0.017611	0.002039	32.8	66.93	1.38	0.2997	0.0066	0.0100	0.0007	64.4
9.1	35	430	12.21	0.6	0.027630	0.002883	51.4	52.11	1.28	0.4160	0.0093	0.0093	0.0012	59.9
9.2	57	398	7.00	0.8	0.034492	0.002761	64.3	59.77	1.24	0.5771	0.0100	0.0060	0.0010	38.4
10.1	87	420	4.81	1.0	0.013854	0.001558	25.8	72.01	1.30	0.2584	0.0051	0.0103	0.0005	66.1
10.2	44	411	9.30	0.6	0.025447	0.002662	47.3	58.69	1.34	0.4184	0.0098	0.0010	0.0010	57.6
11.1	34	369	10.75	0.5	0.027740	0.002921	51.6	54.33	1.34	0.4124	0.0092	0.0089	0.0011	57.2
11.2	45	394	8.75	0.7	0.028876	0.002621	53.7	53.24	1.18	0.5294	0.0107	0.0087	0.0011	55.8
12.2	497	50	0.10	1.6	0.028322	0.001868	52.9	260.51	3.68	0.4760	0.0068	0.0018	0.0002	11.6
13.1	151	8	0.05	1.0	0.034971	0.002753	65.3	136.17	2.38	0.5833	0.0100	0.0025	0.0005	16.4
13.2	48	437	9.05	0.7	0.028979	0.002682	53.9	55.55	1.22	0.4381	0.0083	0.0011	0.0011	53.2
14.1	49	425	8.65	0.7	0.023750	0.002314	44.2	62.23	1.37	0.3423	0.0076	0.0090	0.0008	57.6
14.2	52	447	8.61	0.7	0.024840	0.002444	46.2	61.30	1.32	0.4416	0.0087	0.0088	0.0009	56.3

f<sub>206</sub> % denotes the percentage of <sup>206</sup>Pb that is common Pb.

biotite dehydration melting. Rolland et al. (2009) concluded that a small thermal increase initiated muscovite dehydration melting in the Tangtse area. However, this is unnecessary when considering external water influx. In this case, melting is expected to begin at the water saturated solidus for pelites and quartzofeldspathic rocks, which is essentially similar to that of the haplogranitic system  $Qtz + Ab + Or + H_2O$  with temperatures as low as 650 °C (Clemens and Vielzeuf, 1987; Holtz et al., 1992). Water influx can create significant amounts of melt, depending on the size of the infiltrated (shear-) zone (Mogk, 1992; Genier et al. 2008). Possible sources for infiltrating water are hydrated, low-grade metamorphosed sedimentary rocks of the Karakoram Metamorphic Complex, overthrust by the Pangong Metamorphic Complex (Weinberg and Mark, 2008).

In summary, field relations suggest widespread partial melting of two major rock sequences, meta-sedimentary and calc-alkaline rocks, in the presence of a water-rich fluid contemporaneous with deformation. In the process, a large network of magmatic bodies developed, linking nearly *in situ* leucosomes with a large network of magma sheets and bodies.

## 5. Evidence for magma hybridization in migmatites

In the PMC, different rock types that underwent anatexis are interlayered on the scale of meters to hundreds of meters (Figs. 2, 3). This provides an opportunity for magmas from different sources to interact early in their migration history as they travel through an expanding channel network. In the following, we describe two field examples where this might have happened.

### 5.1. Base of Tangtse Pluton

At the exposed base of the Tangtse Pluton, an irregular sheet of calc-alkaline Bt–granodiorite of the Muglib Batholith border facies intrudes Bt–psammite (Fig. 7). Both rock types have undergone partial melting. This is evidenced in the Bt–psammite by chaotically folded leucosomes and leucosome patches comprised of Ms–Bt ± Grt–leucogranite with melanosome rims consisting mostly of biotite and small amounts of Pl + Qtz + Grt (Fig. 7c, f).

In the Bt–granodiorite sheet anatexis is evidenced by leucosome patches with diffuse boundaries with the melanosome that form an irregular network of Bt ± Grt–leucogranite pockets and veins, feeding into a larger leucosome with width varying up to one meter (Fig. 7b). Although sometimes difficult to distinguish, the neosome is coarser-grained and more felsic than the paleosome. Melanosome rims bordering the leucosome are absent. Isolated rafts of Bt–granodiorite with diffuse boundaries are found in the large leucosome (Fig. 7d). Garnet is heterogeneously distributed in the leucosome and absent in the melanosome except for high concentrations on wispy schlieren of biotite dragged from the Bt–psammite at the contact with the partially molten Bt–granodiorite sheet. The presence of garnet and biotite–garnet schlieren from the Bt–psammite in the leucosome suggests it is a hybrid formed by merging of magma from the Bt–granodiorite with magma from the Bt–psammite. If this is so, then the pre-existing granodiorite gave rise to a magma channelway that was used by leucosomes from both rock types. In order to test this hypothesis, we sampled the different rock types in this and adjoining outcrops to study their isotopic composition.

### 5.2. Leucogranite dykes in the Darbuk–Shyok gorge

In the Darbuk–Shyok gorge (Fig. 1b), mainly pegmatitic Bt ± Ms ± Grt leucogranite dykes cut across interlayered amphibolites and calc-silicate rocks, calc-alkaline diorites of the Muglib Batholith, but also merge continuously with *in situ* leucosomes in dioritic protoliths (Fig. 8). Diorite gneisses show leucosome patches with

euhedral hornblende poikiloblasts and diffuse margins to the melanosome, interpreted to represent *in situ* leucosomes. These leucosomes are generally parallel to tectonic foliation and compositional layering and have melanosome rims consisting of mostly Hbl + Bt, forming a stromatic migmatite. These Hbl-bearing leucosomes are connected with the crosscutting Bt ± Ms ± Grt–leucogranite dykes and, in the field and in thin section, the contact is seamless (Fig. 8b). In parts of this outcrop, large amounts of magma disrupt pre-existing layering in the calc-alkaline protolith and form a diatexite migmatite (Fig. 8c). Continuity between *in situ* leucosome in the dioritic protolith and intrusive dykes suggest contemporaneity of dyke and local anatexis.

## 6. Major and Trace Element Geochemistry

We carried out major and trace element analysis on 88 samples of the main lithologies of the PMC, including 58 leucogranitic samples from the Karakoram Shear Zone and Karakoram Batholith. In general,  $Fe_2O_3t$ , MgO,  $TiO_2$  and CaO contents of source rocks and leucogranites in the Karakoram Shear Zone and Karakoram Batholith correlate negatively with  $SiO_2$ ,  $K_2O$  and  $SiO_2$  show no clear trend. Leucogranites have  $SiO_2$  contents between 64.0 wt% and 76.2 wt% and are dominantly mildly peraluminous (A/CNK 1.02 to 1.16; Fig. 9a). In the alkali–lime vs.  $SiO_2$  diagram (Fig. 9b), the source rocks follow the calc-alkalic to alkali–calcic trend and almost all leucogranite samples lie in the field of peraluminous leucogranites as defined in Frost et al. (2001). The different rock types define different fields depending on their  $Fe_2O_3t + MgO + TiO_2$  content (Fig. 9c). While the ferromagnesian and titaniferous phases are concentrated in the calc-alkaline diorites, Bt–psammite, Bt–pelites and melanosome samples, the calc-alkaline granodiorites and diatexites form an intermediate group. The leucogranites have the lowest  $Fe_2O_3t + MgO + TiO_2$  contents (< 2.15 wt %).  $K_2O$  contents of leucogranites are usually high between 4 and 5 wt%, ranging from 0.94 wt% to 5.63 wt%. High, and variable,  $K_2O$  concentrations suggest K-feldspar accumulation trends in leucogranites. CaO +  $Na_2O$  concentrations in leucogranites range from 3.41 wt % to 9.89 wt % (not shown in Fig. 9).

The high  $K_2O$  content of 10.1 wt% in a leucosome sample of a Muglib Batholith migmatite (sample TNG60d in Table 1) is the result of K-feldspar accumulation in the Hbl-bearing leucosomes in Hbl–Bt diorite (Fig. 3b) in accordance with petrographic observations. Rb correlates positively with  $K_2O$  (Fig. 10a), but not with  $Fe_2O_3t$  and  $TiO_2$ , suggesting that Rb contents are mainly controlled by the amount of K-feldspar and not by muscovite or biotite in the leucogranites. High Ba and Sr concentrations suggest feldspar crystallization leading to relatively quartz-poor but feldspar-rich leucogranites with a cumulate character (Fig. 10b). Feldspar accumulation as a result of Rayleigh fractionation is shown in the calculated trace element contents in the added curves of Fig. 10b. Relatively low Rb contents result in low Rb/Sr ratios, generally below one. The Tangtse Pluton (Fig. 2) appears to be an example of this; a magma that has started to crystallize close to the source.

## 7. Geochronology

In order to constrain the relation between timing of protolith crystallization, anatexis and leucogranite intrusion, we dated zircon and titanite grains from two samples of potential source rocks and two leucogranite samples using U–Pb SHRIMP analysis. We selected a melanosome (sample TNG62a), rich in hornblende and biotite as well as titanite, apatite and zircon. This sample was taken from a migmatized part of the Muglib Batholith ~3 km along strike to the SE of the Tangtse Pluton. The second sample (TNG131a) is a Bt–granodiorite sheet, interpreted as Muglib Batholith border facies, from the outcrop at the base of the Tangtse Pluton in Fig. 7b. For age determination of

**Table 4**  
U–Pb SHRIMP data; sample TNG148a, TNG148b.

Sample TNG148a															
Coordinates		34°03'40.4"N 78°13'52.7"E													
Grain spot	U (ppm)	Th (ppm)	Th/U	<sup>206</sup> Pb* (ppm)	<sup>204</sup> Pb/ <sup>206</sup> Pb	±	f <sub>206</sub> %	<sup>238</sup> U/ <sup>206</sup> Pb	±	<sup>207</sup> Pb/ <sup>206</sup> Pb	±	<sup>206</sup> Pb/ <sup>238</sup> U	±	Radiogenic age (Ma)	
														<sup>206</sup> Pb/ <sup>238</sup> U	±
1.1	208	790	3.80	1.8	0.040139	0.002097	74.9	98.65	4.94	0.6528	0.0315	0.0025	0.0006	16.4	3.7
2.1	352	47	0.13	2.5	0.037675	0.002185	70.3	122.82	1.63	0.5935	0.0060	0.0024	0.0005	15.5	2.9
3.1	237	45	0.19	2.1	0.038220	0.002227	71.3	98.95	1.40	0.6388	0.0068	0.0029	0.0006	18.6	3.7
4.1	158	171	1.08	2.1	0.049082	0.002556	91.6	65.07	0.98	0.7046	0.0074	0.0013	0.0011	8.3	6.8
4.2	474	206	0.44	3.0	0.035915	0.001540	67.1	134.34	1.74	0.5603	0.0054	0.0025	0.0003	15.8	2.2
5.1	305	50	0.16	2.2	0.041903	0.002224	78.3	120.02	1.63	0.6085	0.0064	0.0018	0.0005	11.7	3.2
6.1	455	115	0.25	3.1	0.034043	0.001693	63.6	127.73	1.62	0.5746	0.0061	0.0029	0.0004	18.4	2.3
6.2	262	40	0.15	2.1	0.037824	0.001839	70.6	109.40	1.56	0.6410	0.0071	0.0027	0.0005	17.3	3.0
6.3	127	875	6.88	1.7	0.044925	0.002325	83.8	65.53	1.09	0.6986	0.0088	0.0025	0.0010	15.9	6.1
7.1	357	35	0.10	2.5	0.035071	0.001621	65.5	123.36	1.65	0.5812	0.0060	0.0028	0.0004	18.0	2.4
8.1	254	43	0.17	2.1	0.038986	0.001901	72.8	102.82	1.48	0.6308	0.0071	0.0026	0.0005	17.0	3.3
9.1	249	26	0.11	2.1	0.041786	0.001999	78.0	103.02	1.50	0.6532	0.0077	0.0021	0.0005	13.7	3.5
10.1	221	224	1.01	1.8	0.039211	0.002012	73.2	105.52	1.55	0.6406	0.0075	0.0025	0.0005	16.3	3.3
10.2	207	20	0.10	2.2	0.041973	0.002220	78.3	82.02	1.28	0.6695	0.0083	0.0026	0.0007	17.0	4.6
11.1	185	63	0.34	1.6	0.037226	0.002174	69.5	100.15	1.57	0.6379	0.0083	0.0030	0.0006	19.6	3.5
12.1	252	24	0.09	2.1	0.039991	0.003275	74.7	104.59	1.52	0.6200	0.0072	0.0024	0.0007	15.6	4.5
13.1	220	30	0.13	2.0	0.040177	0.001954	75.0	94.86	1.40	0.6460	0.0073	0.0026	0.0006	17.0	3.7
14.1	527	288	0.55	3.3	0.034685	0.001475	64.8	138.82	1.78	0.5499	0.0054	0.0025	0.0003	16.3	2.1
15.1	209	88	0.42	1.9	0.042656	0.002092	79.6	92.08	1.38	0.6374	0.0075	0.0022	0.0006	14.2	4.0
<b>Zircon analysis</b>															
Zircon included within titanite grains in sample TNG148a															
1.1	3034	1861	0.61	11.6	0.020867	0.002902	35.17	224.30	2.95	0.3245	0.0299	0.0029	0.0002	18.6	1.1
2.1	5655	2607	0.46	14.9	0.001053	0.000248	0.92	326.41	3.52	0.0537	0.0008	0.0030	0.0000	19.5	0.2
Sample TNG148b															
Zircon analyzed <i>in situ</i> in polished thin section															
24–1	1425	4	0.003	3.7	0.004420	0.001228	5.5	329.6	6.0	0.0895	0.0051	0.0029	0.0001	18.5	0.4
24–2	5784	3703	0.64	35.2	0.026992	0.002627	49.8	141.2	2.2	0.4406	0.0144	0.0036	0.0002	22.9	1.0
29–1	2060	1304	0.63	148.2	0.051735	0.000951	96.4	11.941	0.136	0.8127	0.0091	0.0030	0.0018	19.6	11.6
29–2	1464	2858	1.95	5.7	0.020839	0.002127	37.0	222.1	6.8	0.3389	0.0198	0.0028	0.0001	18.3	0.9
29–3	1709	823	0.48	4.4	0.006514	0.001335	8.3	333.7	5.0	0.1121	0.0062	0.0027	0.0000	17.7	0.3
29–4	1251	1503	1.20	163.2	0.054529	0.000701	97.6	6.588	0.073	0.8266	0.0198	0.0036	0.0047	23.1	30.1
47–1	2006	1015	0.51	5.5	0.000608	0.000248	2.2	313.2	4.3	0.0640	0.0020	0.0031	0.0000	20.1	0.3
47–2	672	1095	1.63	1.6	0.001152	0.000628	1.0	362.5	7.4	0.0546	0.0042	0.0027	0.0001	17.6	0.4
47–3	1116	2284	2.05	3.5	0.012479	0.001932	23.2	271.6	4.5	0.2294	0.0075	0.0028	0.0001	18.2	0.4

f<sub>206</sub> % denotes the percentage of <sup>206</sup>Pb that is common Pb.

leucogranites we chose two samples from the Tangtse Pluton, one for zircon and one for titanite analysis (sample TNG148a and TNG148b).

### 7.1. Age of the Muglib Batholith

Zircons from samples TNG62a and TNG131a are prismatic, either translucent or pinkish in colour and between 150 µm and 500 µm in length, on average 200 µm. Cathodoluminescence (CL) imaging shows dominantly oscillatory zoning with little evidence for inherited cores, or overgrowths. These are interpreted to represent igneous zoning. A total of 23 areas have been analyzed on 17 zircon grains from sample TNG62a (melanosome), where 18 analyses form a dominant bell-shaped age probability distribution with a weighted mean <sup>206</sup>Pb/<sup>238</sup>U age of 71.4 ± 0.6 Ma (MSWD = 1.14, Fig. 11a; Table 2). One analysis is slightly older whilst the remaining four analyses and are interpreted to have lost radiogenic Pb; for example analysis 1.1 in Table 2. The mean age of 71.4 ± 0.6 Ma is interpreted to represent a single population indicating the magmatic crystallization age of the Hbl–Bt–granodiorite.

Sample TNG131a corresponds to the Bt–granodiorite border facies that intruded Bt–psammites (Fig. 7b). As for the previous sample, the zircon grains are dominated by relatively simple igneous oscillatory zoning as seen under CL, although some discordant central areas may reflect a more complicated igneous crystallization history. A total of 22 areas were analyzed from 17 zircon grains (Fig. 11b; Table 3). An analysis was also made on a zircon included within a titanite grains

during the same SHRIMP session. It yielded a significantly younger <sup>206</sup>Pb/<sup>238</sup>U date of ~63 Ma but the area has likely lost radiogenic Pb and hence was not included in the following discussion or age calculation. The zircon <sup>206</sup>Pb/<sup>238</sup>U ages are slightly dispersed ranging between ~67 and ~74 Ma. The probability density distribution appears bimodal with a more prominent peak at about 70 Ma and another at about 73 Ma, with some younger analyses considered to reflect radiogenic Pb loss. The older group at ~73 Ma may indicate that there was an early period of magmatic zircon crystallization, but with the dominant zircon having crystallized at 70.5 ± 0.6 Ma (mean weighted <sup>206</sup>Pb/<sup>238</sup>U age of 14 analyses, MSWD = 1.03; Fig. 11b). This age is overlapping within error but slightly younger than the 71.4 ± 0.6 Ma for sample TNG62a, and confirms that both intrusions relate to the same magmatic event.

The titanite grains have a light brown colour, are mostly anhedral to subhedral and are between 100 and 250 µm in diameter. In some grains the BSE images show a faint oscillatory zoning, whereas most grains have irregular internal structures, often with a slightly darker, central phase, irregularly surrounded by a lighter BSE component (Fig. 12b). Twenty four areas have been analyzed on 14 titanite grains (Fig. 13c; Table 3). As is common in metamorphic titanite, there are high amounts of common Pb and so the calculated radiogenic ratios and ages have high uncertainties compared to the U–Pb zircon data. In the Tera–Wasserburg plot of Fig. 13a, discordia lines have been fitted to the common Pb uncorrected data. It can be seen that there is an

**Table 5**  
Rb–Sr and Sm–Nd isotopes.

Sample	Type /location	Coordinates	Rb ppm	Sr ppm	<sup>87</sup> Rb/ <sup>86</sup> Sr	<sup>87</sup> Sr/ <sup>86</sup> Sr	Sm ppm	Nd ppm	<sup>147</sup> Sm/ <sup>144</sup> Nd	<sup>143</sup> Nd/ <sup>144</sup> Nd	εNd now	<sup>87</sup> Sr/ <sup>86</sup> Sr at 18 Ma	<sup>143</sup> Nd/ <sup>144</sup> Nd at 18 Ma	εNd <sub>i</sub> at 18 Ma
TNG 71a	Grt–Ms–Bt leucogranite, Tangtse Pluton	34°03'42.6"N 78°13'52.2"E	157.72	406.39	1.123	0.71066	0.65	3.21	0.1224	0.51233	–6.05	0.7104	0.51231	–5.9
TNG 71b	Ms–Bt leucogranite, Tangtse Pluton	34°03'42.6"N 78°13'52.2"E	131.43	455.57	0.835	0.71048	1.20	6.92	0.1048	0.51234	–5.79	0.7103	0.51233	–5.6
TNG148a	Bt leucogranite, Tangtse Pluton	34°03'40.4"N 78°13'52.7"E	145.57	1046.06	0.403	0.70993	2.94	18.36	0.0966	0.51231	–6.42	0.7098	0.51230	–6.2
TNG148b	Bt leucogranite, Tangtse Pluton	34°03'40.4"N 78°13'52.7"E	149.88	1528.89	0.284	0.70868	4.45	29.30	0.0917	0.51235	–5.58	0.7086	0.51234	–5.3
TNG 131 g	Pegmatitic leucosome, Tangtse Pluton	34°03'38.8"N 78°13'52.1"E	119.76	351.52	0.986	0.70904	0.50	2.51	0.1202	0.51244	–3.80	0.7088	0.51243	–3.6
TNG170*	Leucosome, Tangtse gorge	34°02'35.6"N 78°13'16.0"E	52.14	1089.96	0.138	0.70544	0.53	2.97	0.1071	0.51268	0.90	0.7054	0.51267	1.1
TNG186	Leucogranite dyke, Darbuk–Shiyok gorge	34°08'41.8"N 78°08'17.8"E	140.62	438.78	0.926	0.71234	4.53	29.49	0.0929	0.51239	–4.76	0.7121	0.51238	–4.5
TNG187a	Pegmatite dyke, Darbuk–Shiyok gorge	34°08'48.6"N 78°08'26.9"E	109.87	73.56	4.322	0.70979	0.42	0.93	0.2757	0.51242	–4.34	0.7087	0.51238	–4.5
TNG187b	Pegmatite dyke, Darbuk–Shiyok gorge	34°08'48.6"N 78°08'26.9"E	131.98	98.23	3.888	0.70968	1.80	5.73	0.1902	0.51241	–4.37	0.7087	0.51239	–4.4
AGH23a*	Hbl-bearing leucosome, Nubra Valley	34°25'10.6"N 77°49'23.5"E	151.40	903.40	0.485	0.70897	14.35	81.59	0.1064	0.51228	–7.02	0.7088	0.51227	–6.8
AGH25a	Grt–Ms–Bt leucogranite, Nubra Valley	34°27'04.4"N 77°45'53.1"E	158.44	155.61	2.946	0.70831	1.99	12.03	0.1003	0.51235	–5.60	0.7076	0.51234	–5.4
NBR1b*	Ms–Bt leucogranite, Nubra Valley	34°29'06.0"N 77°44'20.0"E	201.14	363.24	1.600	0.70809	2.86	16.05	0.1079	0.51234	–5.80	0.7077	0.51233	–5.6
NBR2a*	Ms–Bt leucogranite, Nubra Valley	34°37'54.6"N 77°38'24.1"E	208.66	501.35	1.203	0.70855	4.44	24.47	0.1097	0.51230	–6.66	0.7082	0.51228	–6.5
NBR3b*	Ms–Bt leucogranite, Nubra Valley	34°46'27.5"N 77°32'45.7"E	201.27	336.80	1.727	0.70863	3.55	20.27	0.1060	0.51226	–7.32	0.7092	0.51225	–7.1
TNG 62a	Melanosome, SW Muglib	34°02'16.8"N 78°14'57.7"E	122.37	538.39	0.658	0.70783	7.30	43.29	0.1019	0.51266	0.37	0.7077	0.51265	0.6
TNG128	Calc-alkaline Hbl–Bt–granodiorite, SW Muglib	33°59'08.3"N 78°18'37.8"E	120.43	575.26	0.605	0.70523	5.41	32.32	0.1011	0.51266	0.43	0.7051	0.51265	0.6
TNG169a*	Calc-alkaline diorite, Tangtse gorge	34°02'40.3"N 78°13'07.8"E	49.42	547.63	0.261	0.70528	3.18	13.46	0.1428	0.51275	2.17	0.7052	0.51273	2.3
TNG98a	Calc-alkaline Hbl–Bt–granodiorite, Darbuk–Shiyok gorge	34°09'23.1"N 78°08'52.0"E	116.76	573.49	0.589	0.70562	5.48	35.28	0.0939	0.51267	0.53	0.7055	0.51265	0.8
AGH5*	Calc-alkaline gabbro, Pangong Range	34°18'47.7"N 77°52'03.8"E	26.52	497.28	0.154	0.70421	3.63	15.39	0.1427	0.51276	2.28	0.7042	0.51274	2.4
TNG 70a	Bt–psammite, Tangtse Pluton	34°03'41.6"N 78°13'53.2"E	255.15	250.40	2.949	0.71251	5.35	28.11	0.1150	0.51214	–9.81	0.7118	0.51212	–9.6
TNG 131d	Bt–psammite, Tangtse Pluton	34°03'38.8"N 78°13'52.1"E	183.68	155.69	3.416	0.71700	6.21	32.64	0.1148	0.51211	–10.22	0.7161	0.51210	–10.0
TNG 112	Pelite, Shiyok Valley	34°12'19.6"N 78°07'55.9"E	168.65	299.82	1.628	0.71188	6.45	32.52	0.1198	0.51212	–10.10	0.7115	0.51211	–9.9
PNG03b	Pelite, Tangtse Valley	33°57'53.5"N 78°23'46.0"E	168.22	147.66	3.299	0.71698	5.44	29.33	0.1120	0.51212	–10.12	0.7161	0.51211	–9.9
TNG108c	Amphibolite, Darbuk–Shiyok gorge	34°08'42.0"N 78°08'18.5"E	4.04	125.56	0.093	0.70477	2.40	6.92	0.2098	0.51309	8.82	0.7047	0.51307	8.8
LEH40**	Ladakh Batholith, Leh	not available		0.339	0.339	0.70485	3.13	14.21	0.1331	0.51267	0.66	0.7048	0.51266	0.8
LEH55**	Ladakh Batholith, Leh	159.00	95.00	4.843	0.70782	1.10	5.86	0.1131	0.51262	–0.29	0.7066	0.51261	–0.1	
LEH29**	Ladakh Batholith, Leh	49.00	219.00	0.647	0.70465	1.87	9.81	0.1152	0.51274	1.93	0.7045	0.51272	2.1	
LEH38a**	Ladakh Batholith, Gyamsa	85.00	119.00	2.066	0.70555	1.69	11.51	0.0888	0.51270	1.27	0.7050	0.51269	1.5	
LEH38b**	Ladakh Batholith, Gyamsa	79.00	188.00	1.216	0.70545	5.30	22.64	0.1416	0.51272	1.54	0.7051	0.51270	1.7	
LEH52**	Ladakh Batholith, Gyamsa	30.40	350.00	0.251	0.70485	8.49	36.85	0.1392	0.51270	1.13	0.7048	0.51268	1.3	

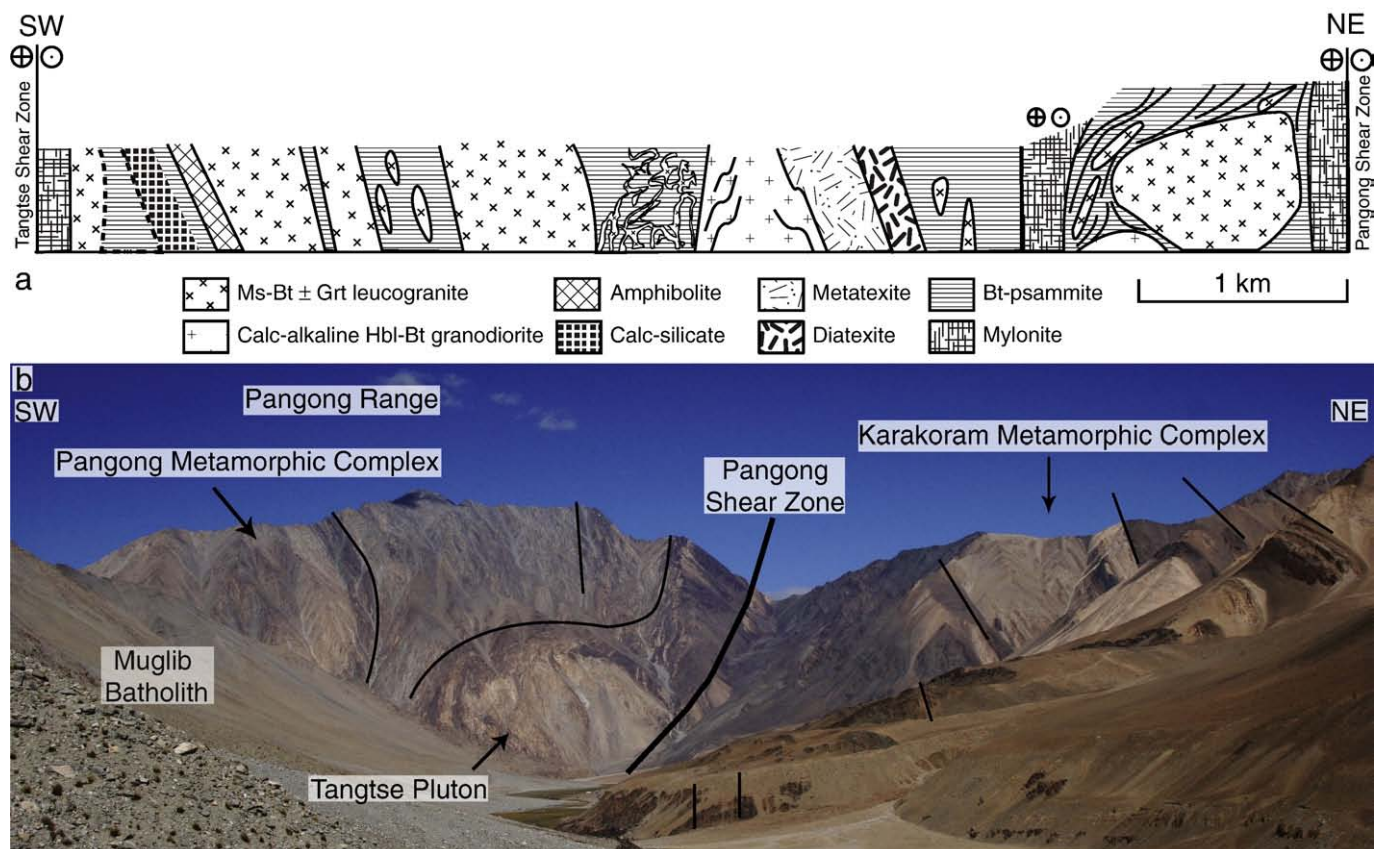


**Fig. 2.** (a) Schematic cross section through the Tangtse gorge roughly perpendicular to strike of the Karakoram Shear Zone. The Tangtse Shear Zone separates the Pangong Metamorphic Complex (PMC) from the Ladakh Batholith to the SW. The Pangong Shear Zone bounds the PMC from the Karakoram Metamorphic Complex to the NE. (b) Photograph of the NE end of the Tangtse gorge (looking NW). Calc-alkaline Muglib Batholith (lower left) and leucogranitic Tangtse Pluton (centre) in the Pangong Range. The Tangtse Pluton intrudes Bt-psammities of the PMC. Grt–St–Hbl–schists and marbles (bright colors) of the upper greenschist/lower amphibolite facies Karakoram Metamorphic Complex (KMC) were overthrust by the PMC during dextral compressive movement.

older grouping that forms a linear array, intersecting the concordia at  $65 \pm 3$  Ma. A second, sub-parallel group is slightly younger ( $\sim 55$  Ma), and then other analyses range down to  $\sim 11$  Ma. The oldest calculated age is younger than that calculated from zircons of the same sample, the likely true magmatic age, and either is spurious or relates to a cooling event post initial magmatism. An early metamorphic event due to continued calc-alkaline intrusion is also possible. The relative probability plot of common Pb corrected  $^{206}\text{Pb}/^{238}\text{U}$  ages highlights the two older age components with a scattered younger cluster peaking between  $\sim 11$  and 21 Ma (Fig. 13c). It is not possible to calculate a meaningful age date for this younger, metamorphic titanite, but it is indicative of a metamorphic crystallization event broadly contemporaneous with anatexis (see below).

#### 7.2. Age of the leucogranites from the Tangtse Pluton

Initially zircons were not recovered from the standard mineral separation applied to sample TNG148a. Titanites were separated similarly to the Bt–granodiorite sample. They have a light brown colour, are mostly anhedral to subhedral and are between 100 and 250  $\mu\text{m}$  large. BSE images show weak oscillatory zoning, more common than in titanites from sample TNG131a, while irregular structures are not as prominent. We interpret the BSE internal structure to reflect compositional differences during magmatic growth as opposed to core and rim structures. Zircon inclusions are common. A total of 19 areas on 15 titanite grains from sample TNG148a have been analyzed (Fig. 13d; Table 4). The analyses are

significantly enriched in common Pb with many measured  $^{207}\text{Pb}/^{206}\text{Pb}$  ratios  $\geq 0.55$ , and ranging to  $\sim 0.70$ . Interpolation to a radiogenic end-member is therefore tenuous. However, it is possible to calculate a 3-dimensional linear fit to this common Pb enriched data and this provides a lower intercept at  $16.7 \pm 1.0$  Ma (MSWD = 1.4, 19 analyses). A weighted mean of common Pb corrected  $^{206}\text{Pb}/^{238}\text{U}$  ages gives  $16.4 \pm 1.4$  Ma (MSWD = 0.4, 19 analyses). Two zircon inclusions within the same titanite separate were also analyzed (Table 4), and have  $^{206}\text{Pb}/^{238}\text{U}$  ages of  $18.6 \pm 1.1$  Ma and  $19.5 \pm 0.2$  Ma, respectively. These zircon grains have very high U concentrations  $\sim 3000$  ppm and  $\sim 5650$  ppm, respectively, and so the radiogenic  $^{206}\text{Pb}/^{238}\text{U}$  ages are unreliable by SHRIMP (see Williams and Hergt, 2000).

From a second sample from the same outcrop (TNG148b), nine areas on 3 zircon grains were analyzed *in situ* in a polished thin section. As with the zircon included within the titanite, the U concentrations range to very high values ( $\sim 5785$  ppm). However, lower, more reasonable U concentrations are recorded, and 5 analyses with  $\leq 1710$  ppm U have a weighted mean  $^{206}\text{Pb}/^{238}\text{U}$  age of  $18.0 \pm 0.4$  Ma (MSWD = 1.09, Fig. 13e; Table 4). It should be noted that the zircon grain with  $\sim 3000$  ppm U that is included in titanite has a  $^{206}\text{Pb}/^{238}\text{U}$  age within uncertainty of the titanite age. Thus, overall the zircon records a slightly older age than that obtained from titanite with high common Pb.

#### 8. Rb–Sr and Sm–Nd isotope geochemistry

In order to track the origin and mixing of magmas from different sources as inferred in the field, we analyzed Rb–Sr and Sm–Nd

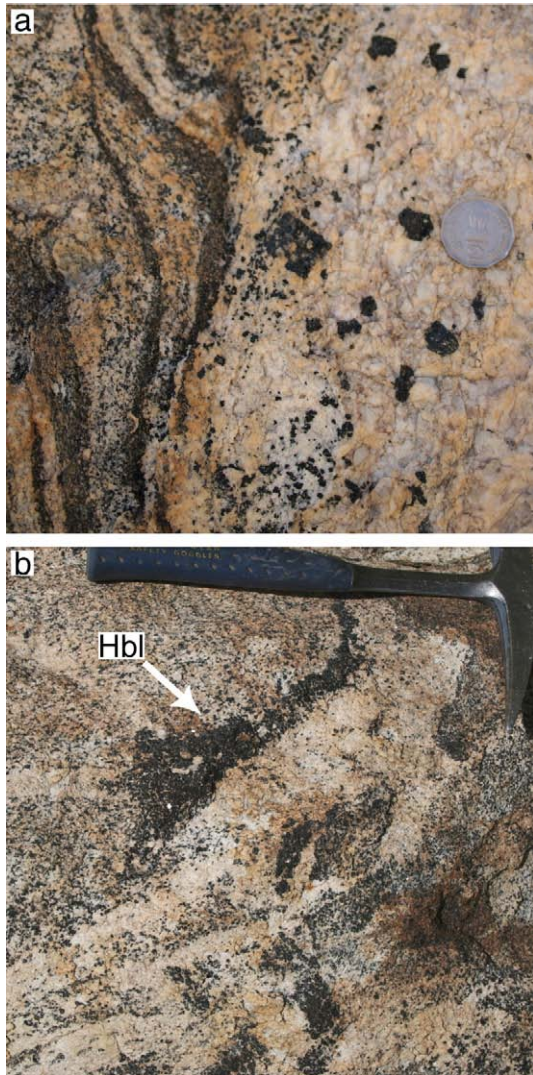


**Fig. 3.** (a) Up to ~1 cm poikilitic hornblende crystals in leucosome in metatextite. (b) Accumulation of hornblende crystals in leucosome network in calc-alkaline Hbl–Bt–granodiorite of the Muglib Batholith.

isotopes of rocks that we interpret to represent magma sources and those that represent melting products, i.e. the leucogranites. We used 18 Ma for recalculation of initial  $^{87}\text{Sr}/^{86}\text{Sr}$  and  $^{143}\text{Nd}/^{144}\text{Nd}$  ratios for leucogranites. This is the most likely crystallization age based on U–Pb



**Fig. 4.** Leucosomes in folded amphibolite. Melt must have been present at the time of deformation, because the folded layer-parallel leucosome cuts across the fold limb but stays in continuity with layer-parallel leucosomes on the opposite limb.



**Fig. 5.** Shear band in stromatic migmatite developed in calc-alkaline diorite. A leucosome forms within the shear band that runs from the upper left to the lower right. Layer-parallel leucosomes have diffuse boundaries with the leucosome in the shear band in the central part. The dark layer (melanosome) in the upper part of the photograph (tip of hammer) is continuous across the shear zone. The thick coarse-grained layer-parallel leucosome in the lower part of the photograph is nearly truncated by the shear zone, indicating that it formed earlier. However, the thinned out right part of the leucosomes almost connects to the counterpart on the left hand side.

SHRIMP data for such rocks (Searle et al., 1998 and our new analyses). For direct comparison with the products of anatexis, we also calculated the isotope data of source rocks and those of the Ladakh Batholith to that time.

### 8.1. Results

Initial  $^{87}\text{Sr}/^{86}\text{Sr}$  between 0.7042 and 0.7077 and initial  $\epsilon_{\text{Nd}}$  values between 0.6 and 2.4 for calc-alkaline granitoids of the Muglib Batholith indicate a mantle origin with a slight crustal influence, or juvenile crustal sources (Table 5, Fig. 14). For comparison we analyzed six samples from the Ladakh Batholith close to Leh (Fig. 1a). These yielded essentially identical  $^{87}\text{Sr}/^{86}\text{Sr}_i$  ranging between 0.7045 and 0.7066 and  $\epsilon_{\text{Nd}_i}$  ranging between  $-0.1$  and 2.1. The overlap with the values for the Muglib Batholith indicates a possible genetic relationship (see discussion below). In contrast, meta-sedimentary rocks of the PMC yielded  $^{87}\text{Sr}/^{86}\text{Sr}_i$  between 0.7115 and 0.7161 that indicate longer crustal residence and  $\epsilon_{\text{Nd}_i}$  that show limited variation between  $-10.0$  and  $-9.6$  (Table 5, Fig. 14). Thus, the protoliths recognized in the field have significantly different isotopic compositions.

The leucogranites, including *in situ* leucosomes interpreted to represent melt products in the PMC have  $^{87}\text{Sr}/^{86}\text{Sr}_i$  ranging from 0.7086 to 0.7121, and  $\epsilon_{\text{Nd}_i}$  values between  $-3.6$  and  $-6.2$ . Similar values were obtained for four Ms–Bt  $\pm$  Grt–leucogranite samples from the Karakoram Batholith collected in the Shyok and Nubra River confluence area and in the Nubra Valley (Fig. 1a) at approximately

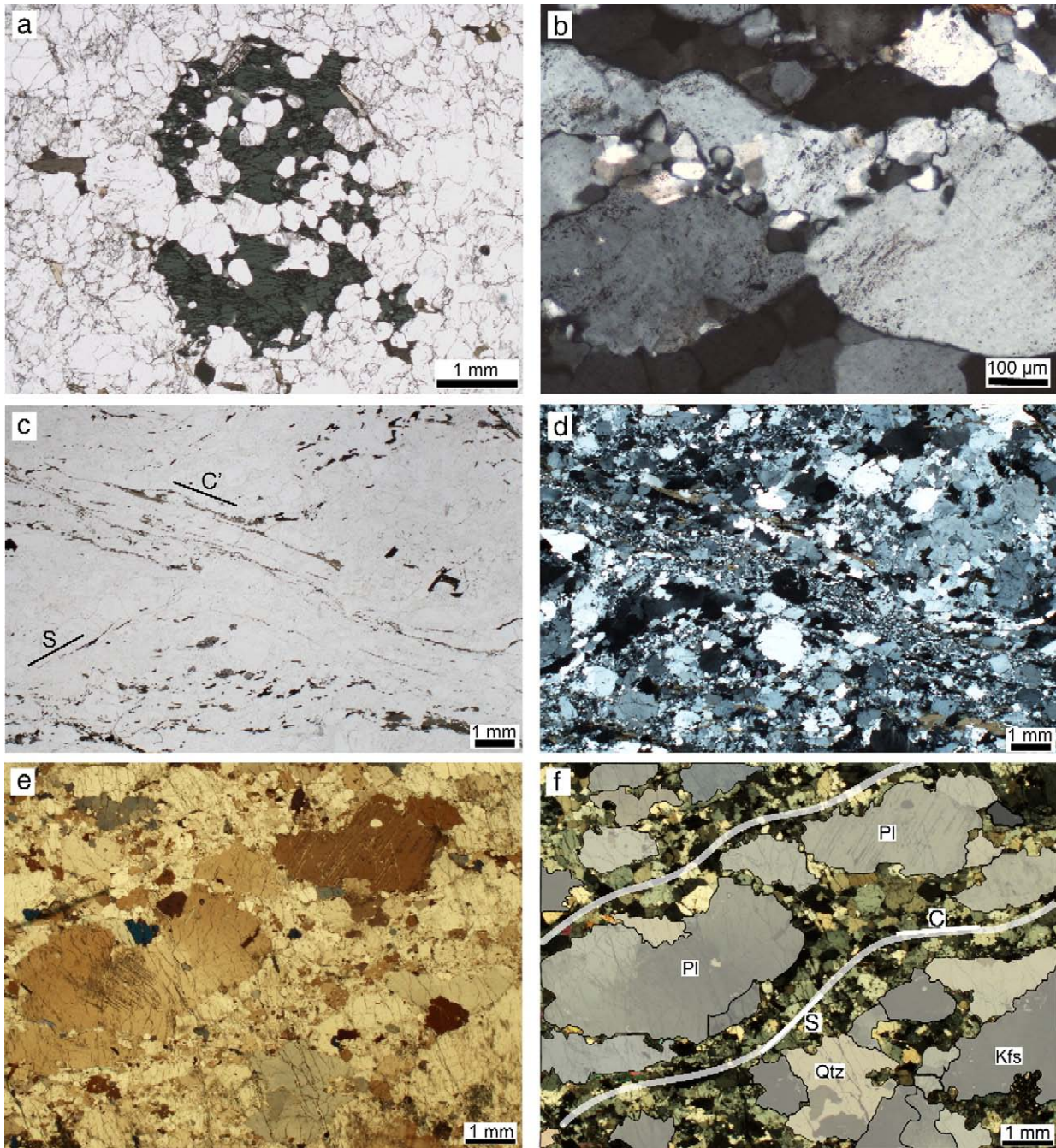


**Fig. 6.** Photomicrographs. (a) Hornblende crystal in tonalitic leucosome of a diatexite in the Tangtse gorge. The poikilitic texture suggests that the hornblende is peritectic. Plane-polarized light. (b) Recrystallization of deformed K-feldspar grains in a shear band in Bt±Grt leucogranite. Cross-polarized light. (c) and (d) C-type shear band in Bt±Grt leucogranite indicating dextral shear sense. Plane-polarized light and cross-polarized light, respectively. (e) Plagioclase and K-feldspar phenocrysts and fine-grained Qtz, Pl and Kfs in Grt–Ms–Bt leucogranite. Polarizer is only half turned in. (f) Same as in (e) but with crossed polarizer and line drawing to illustrate that the fine grains define a dextral C–S fabric. This fabric is interpreted to have been developed before complete crystallization of the magma.

60 km, 65 km, 85 km and almost 100 km distance from the Tangtse gorge ( $^{87}\text{Sr}/^{86}\text{Sr}_i = 0.7076$  to  $0.7092$  and  $\epsilon_{\text{Nd}i} = -5.4$  to  $-7.1$ ). In the region of Rongdu (Fig. 1a) in the Shyok Valley, we have mapped a kilometer-wide Hbl–leucogranite body within the Karakoram Batholith similar in field appearance to Hbl-bearing leucosomes of the Tangtse migmatites. An enclave of calc-alkaline diorite migmatite was collected from within this body. Analysis of the hornblende-bearing leucosome of this sample (AGH23a in Table 5), which is petrographically and geochemically comparable to leucosomes in Hbl–Cpx diorites of the Muglib Batholith close to Muglib (sample TNG60d in Table 1), yielded isotope values similar to those of the Karakoram Batholith.

In the  $\epsilon_{\text{Nd}i}$  vs.  $^{87}\text{Sr}/^{86}\text{Sr}_i$  diagram (Fig. 14), leucogranites from the PMC and the Karakoram Batholith define a field with intermediate values between those of the calc-alkaline granitoids and meta-sedimentary rocks. In a simple two end-member mixing calculation, this field lies within hyperbolic curves between samples we infer to be representative of source rocks (Fig. 14). While  $\epsilon_{\text{Nd}i}$  values of leucogranites show only little variation,  $^{87}\text{Sr}/^{86}\text{Sr}_i$  scatter over a wider range.

Like the majority of leucogranite samples analyzed, those collected from the two outcrops described above (Figs. 7 and 8) also yielded intermediate signatures between those of calc-alkaline granitoids and meta-sedimentary rocks. The pegmatitic leucosome in the outcrop in

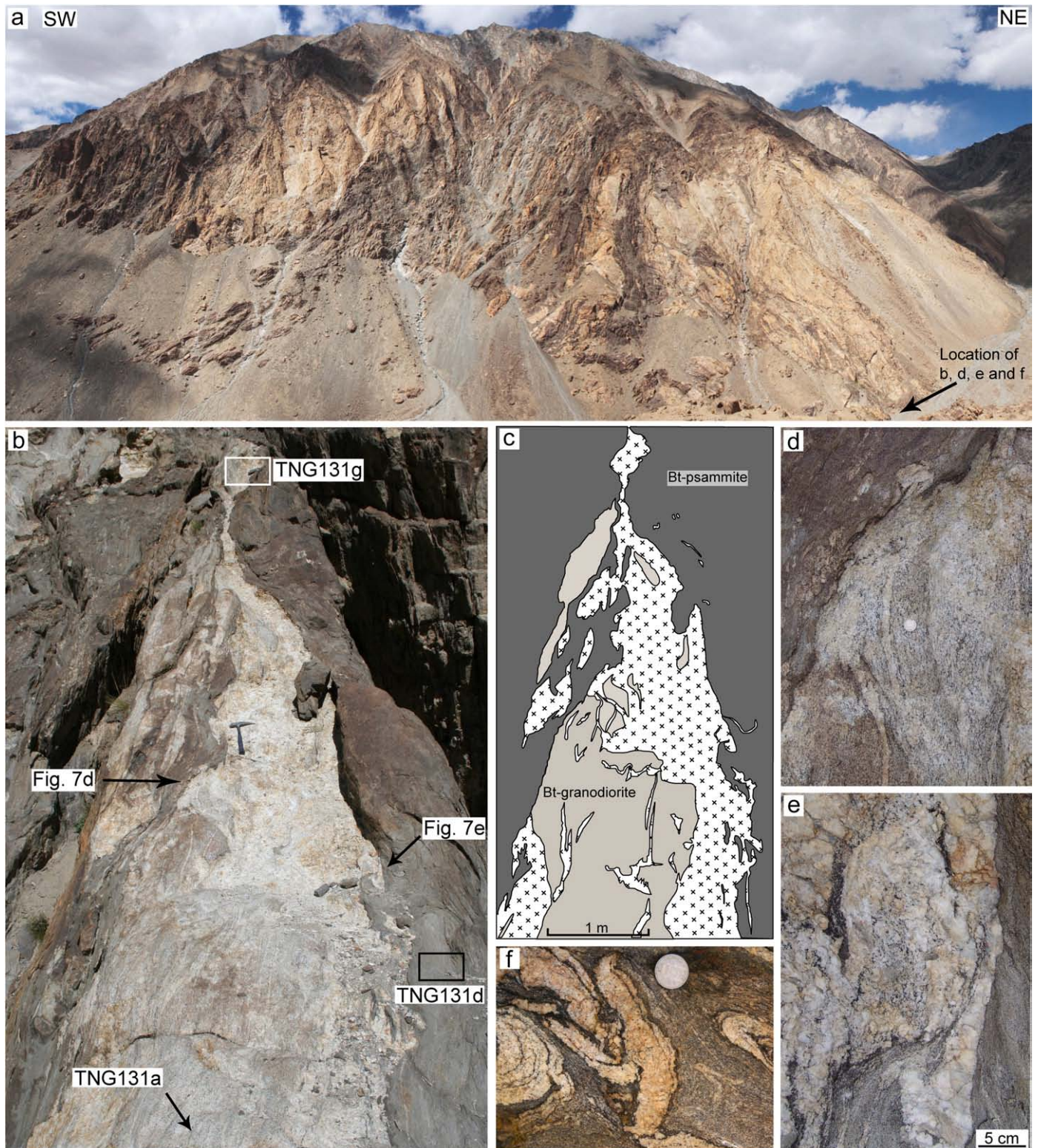


**Fig. 7.** Outcrops at the base of the Tangtse Pluton indicative of magma hybridization in the source. (a) Pangong Injection Complex and Tangtse Pluton looking NW. Dark rocks are Bt-psammites of the PMC, and light rocks are leucogranites. (b) Migmatite outcrop at the foot of the Tangtse Pluton. Leucosomes in a calc-alkaline Bt-granodiorite (lower centre; sample TNG131a: Zircon age =  $70.5 \pm 0.6$  Ma) show diffuse boundaries with the leucosome (sample TNG131g, Table 2) in the centre of the photo which is connected to the leucogranite sheets that form the Tangtse Pluton. The surrounding Bt-psammite (sample TNG131d, Table 2) is also migmatitic. (c) Line drawing of (b). (d) Detail of (b); *In situ* leucosomes in Bt-granodiorite merge with the large pegmatitic leucosome. The Bt-granodiorite also forms rafts (towards right side of photograph). (e) Detail of (b); entrained wispy schlieren of Bt-psammite containing garnet. (f) Detail of folded leucosomes in Bt-psammite. Thin melanosome rims around leucosomes consist mostly of biotite.

Fig. 7b (sample TNG131g in Table 5) yielded a  $^{87}\text{Sr}/^{86}\text{Sr}_i$  of 0.7088, and a  $\epsilon_{\text{Nd}_i}$  value of  $-3.6$ . These are similar to isotope values obtained from two Ms-Bt  $\pm$  Grt-leucogranite samples from leucogranite sheets such as in

Fig. 7c (TNG71a and TNG71b in Table 5) and two other Bt-leucogranite samples from the Tangtse Pluton close to the outcrop in Fig. 7 (TNG148a and TNG148b in Table 5).



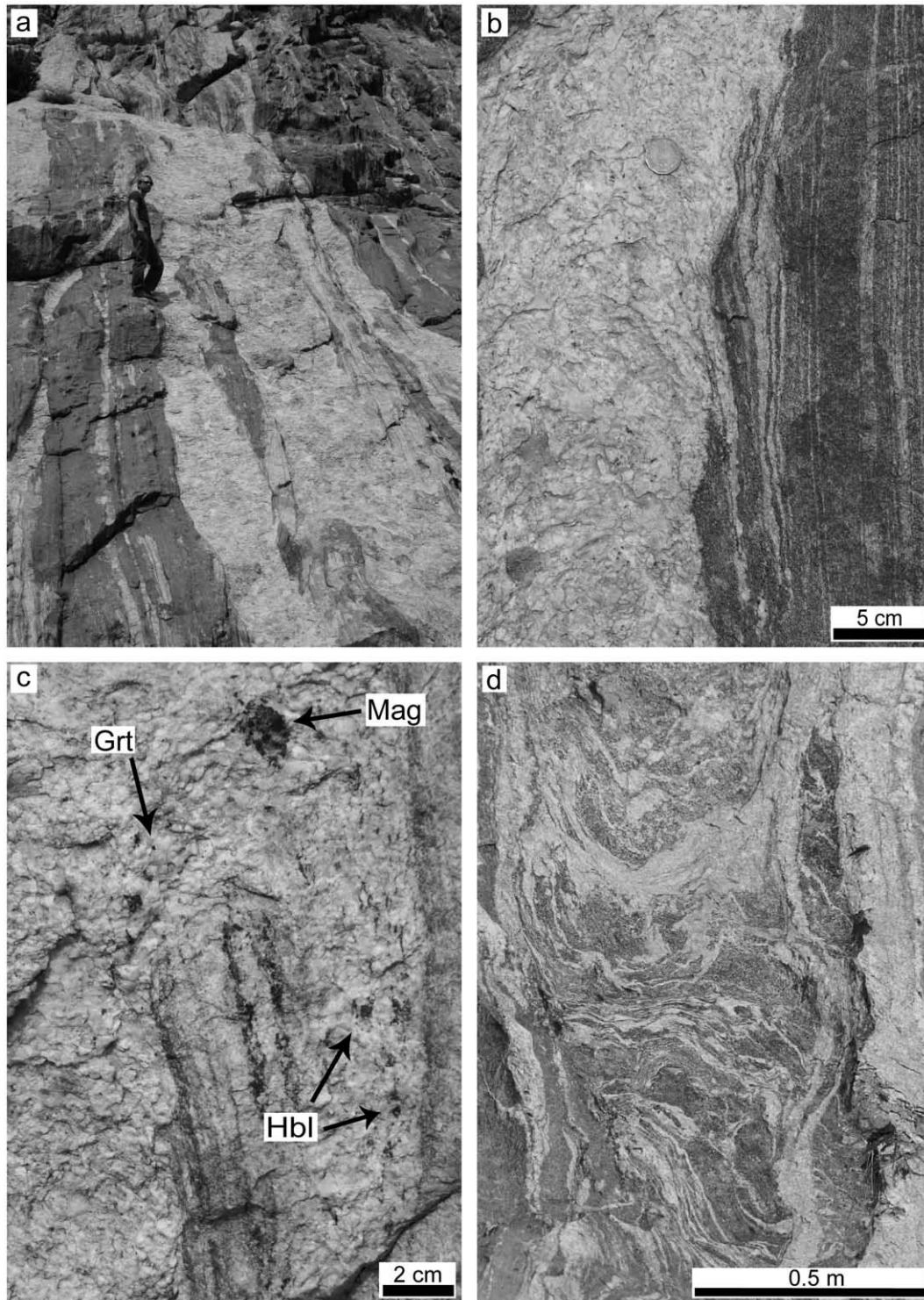


**Fig. 8.** (a) Pegmatitic leucogranite dykes intrude Hbl–Bt–gneiss in the Darbuk–Shyok gorge (samples TNG187a and TNG187b in Table 2). (b) Continuity between layer-parallel *in situ* Hbl-bearing leucosomes and crosscutting large garnet-bearing leucogranite dyke. *In situ* leucosomes generally have thin melanosome rims and are sometimes connected to leucosomes patches that have diffuse boundaries to the melanosome. (c) Seamless merging between dyke and *in situ* Hbl-bearing leucosome. Garnet crystals and cluster of magnetite in pegmatitic Grt–Bt–leucogranite dyke. The dyke continues to the upper left side of the photograph. (d) Diatexite migmatite. The pegmatitic leucogranite dyke that borders the diatexite migmatite is continuous with leucosomes in migmatite.

The isotope values of samples from two pegmatitic Grt–Ms–Bt–leucogranite dykes from the outcrop in Fig. 8 (TNG187a, TNG187b in Table 5) also show intermediate values ( $^{87}\text{Sr}/^{86}\text{Sr}_i = 0.7087$  for both samples,  $\epsilon_{\text{Nd}_i} = -4.5$  and  $-4.4$ , respectively). A Ms–Bt leucogranite dyke (TNG186 in Table 5) that intrudes calc-silicate rocks close by, has a comparable  $\epsilon_{\text{Nd}_i}$  value of  $-4.5$ , but a remarkably high  $^{87}\text{Sr}/^{86}\text{Sr}_i$  of 0.7121.

Whilst the majority of leucosomes show this intermediate signature, a Ms–Bt leucogranite sample (TNG170, Table 5) collected from within a metatexite in the centre of the Tangtse gorge has isotope values close to those for a patchy melanosome in diorite ( $^{87}\text{Sr}/^{86}\text{Sr}_i = 0.7052$  and  $\epsilon_{\text{Nd}_i} = 2.3$ ) in the same outcrop (TNG169a in Table 5). These values are similar to those of the calc-alkaline source rocks ( $^{87}\text{Sr}/^{86}\text{Sr}_i = 0.7054$  and

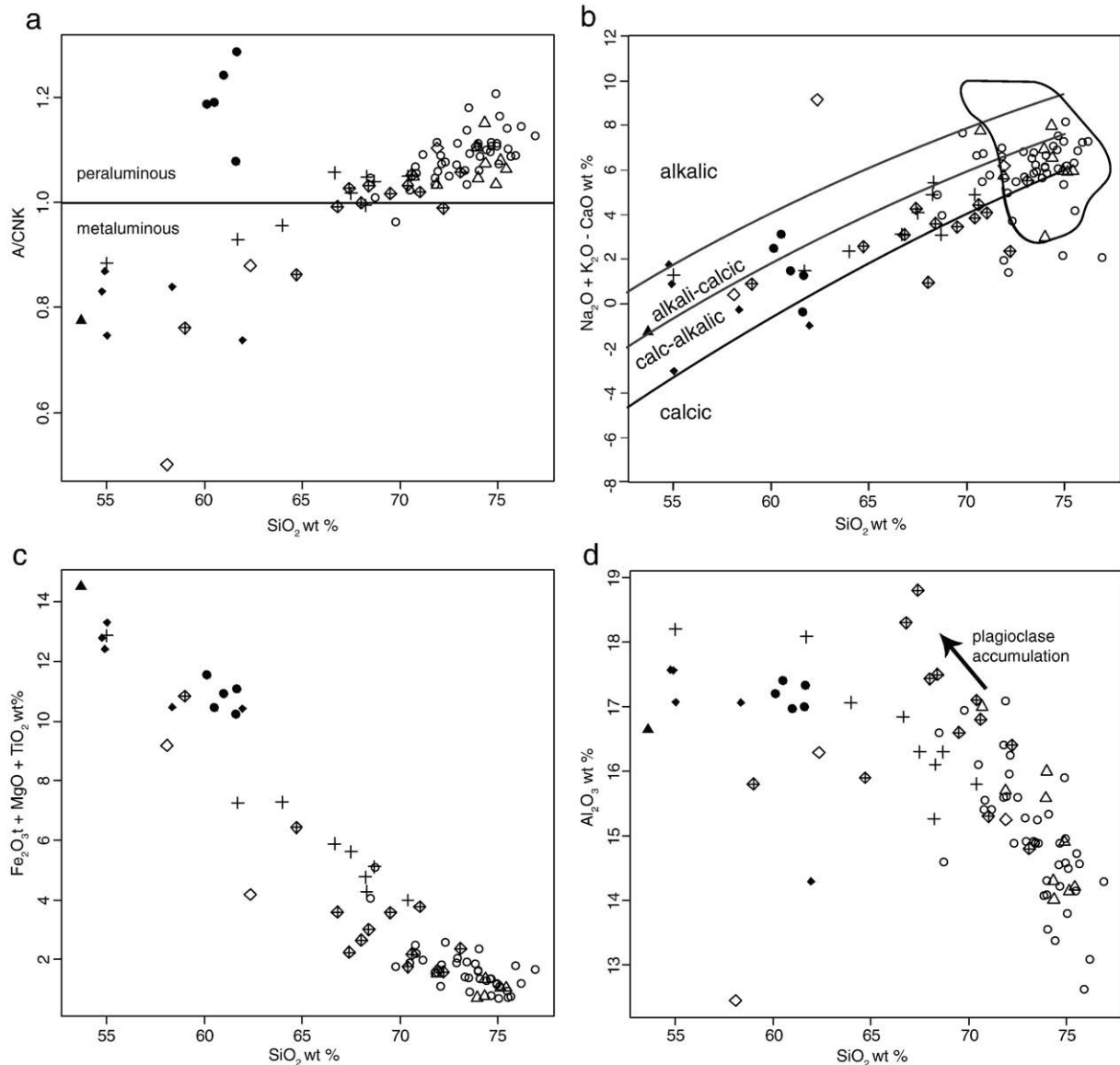


**Fig. 9.** Variations of major element concentrations of whole rock samples expressed as oxide weight percent. See explanations in text. (b) Alkali-lime vs.  $\text{SiO}_2$  diagram after Frost et al. (2001). Rocks of the PMC that show no signs of anatexis are not included. Filled triangle: amphibolite gneiss (possibly andesitic protolith); filled diamonds: calc-alkaline diorites; filled circles: Bt-psammities and Bt-pelites; crosses: calc-alkaline granodiorites; open diamonds with crosses: diatexites; open triangles: pegmatitic leucogranite dykes; open diamonds: Hbl-Kfs leucosome; open circles: leucogranites. The arrow in (d) indicates plagioclase accumulation.  $N=87$ .

$\epsilon_{\text{Nd}_i} = 1.1$ ), and indicates that in this particular case the leucosome was not hybridized.

An exceptional amphibolite gneiss sample ( $\text{SiO}_2 = 52.82$  wt %) of the PMC (TNG108c in Table 5) has an isotope signature ( $^{87}\text{Sr}/^{86}\text{Sr}_i = 0.7047$ ,  $\epsilon_{\text{Nd}_i} = 8.8$ ) close to the field of present-day prevalent mantle (Zindler and Hart, 1986). This sample is isotopically and geochemically comparable to Kohistan-Ladakh island arc lavas (Northern Group, type 2 lavas in Rolland et al. 2002).

## 9. Discussion

### 9.1. Geochemical characteristics: comparison to other Miocene Himalayan leucogranites

Leucogranites of the broader Karakoram region are remarkably different from the High Himalayan leucogranites studied in Nepal (e.g. Deniel et al., 1987; Le Fort et al., 1987). High Himalayan leucogranites are generally strongly peraluminous, have high Rb/Sr ratios and high  $^{87}\text{Sr}/^{86}\text{Sr}$  (0.74–0.82), whereas Karakoram leucogranites are mildly

peraluminous, have low Rb/Sr ratios and  $^{87}\text{Sr}/^{86}\text{Sr}$  (0.71 to 0.72; Crawford and Windley, 1990). The leucogranites we studied in the Karakoram Shear Zone are geochemically comparable to the latter with A/CNK between 1.02 and 1.16, Rb/Sr ratios on average below one, and  $^{87}\text{Sr}/^{86}\text{Sr}_i$  (0.7086 to 0.7121). Muscovite dehydration melting leads to high Rb/Sr ratios in the melt (Inger and Harris, 1993), whereas the low Rb/Sr ratios of the Karakoram rocks are most likely the result of  $\text{H}_2\text{O}$ -fluxed melting because plagioclase will melt preferably over biotite or muscovite (Patiño Douce and Harris, 1998).

### 9.2. Significance of water-fluxed melting

The significance of water-fluxed melting synchronous with deformation for crustal differentiation has been discussed for the European Alps (e.g. Burri et al., 2005; Berger et al., 2008). Most experimental work in the literature has been undertaken for fluid absent conditions where the limiting factor for melt production is the abundance of water-bearing phases, e.g. muscovite, in the source rock (see discussion in Clemens, 2006). This is in contrast with water-fluxed melting, where the

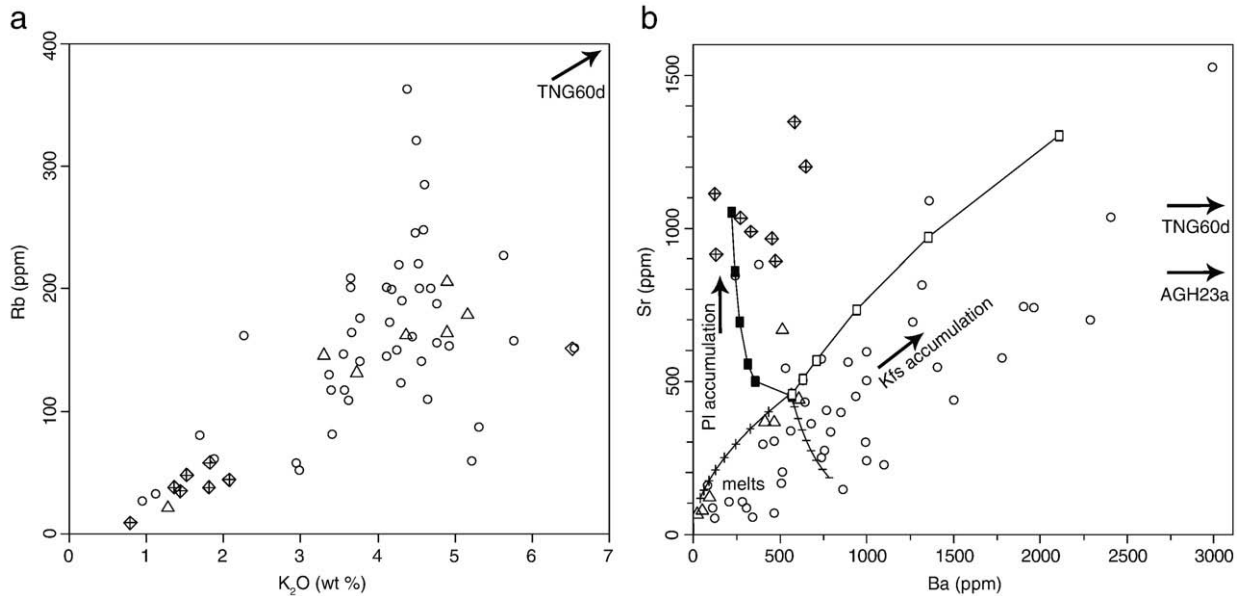


**Fig. 10.** (a) Rb contents correlate positively with K<sub>2</sub>O in leucogranites, interpreted as the result of K-feldspar accumulation. Sample TNG60d (Hbl-Kfs leucosome) with extremely high K<sub>2</sub>O (10.1wt.%) and Rb (441 pm) concentrations is not shown (N=60). (b) Ba vs. Sr in leucogranites. High Ba and Sr concentrations indicate feldspar cumulates. The Hbl-Kfs leucosome samples TNG60d (Ba=8280 ppm and Sr=1083 ppm) and AGH23a (Ba=4136 ppm and Sr=903 ppm) are not shown for scaling reasons. The curves represent model calculations for fractionation and accumulation. Starting composition is leucosome TNG71b (Ba=565 ppm and Sr=448 ppm). Plus and minus symbols represent modelled compositions of residual liquids after Raleigh fractionation of K-feldspar and plagioclase, respectively, in 5% increments (5%, 10%, 15%... fractionated minerals). Open and filled squares represent modelled compositions of cumulates after Raleigh fractionation of K-feldspar and plagioclase, respectively, for different degrees of accumulation F=0.1...0.8. Partition coefficients (Kd) after Arth (1976). Calculation after Rollinson (1993). See Fig. 9 for symbols. N=59.

availability of free water is the main limiting factor and melting would continue as long as water is brought into the system, for example via a shear zone (e.g. Mogk, 1992; Genier et al., 2008). In the Karakoram Shear Zone these processes operate on a large scale, potentially giving rise to magma volumes of batholith dimensions.

### 9.3. Age relations between leucogranites and the Muglib Batholith

Titanite and zircon grains from the two leucogranite samples dated yielded slightly different ages: 16.4 ± 1.4 Ma for titanite (sample TNG148a; Fig. 13d), compared to 18.0 ± 0.4 Ma for zircon (sample TNG148b; Fig. 13e). Because the titanite is strongly enriched in common Pb and hence less reliable, we consider the 18.0 ± 0.4 Ma zircon age as most closely reflecting the crystallization age of the Tangtse Pluton. Despite the slight differences, the two results overlap within error. However, ID-TIMS zircon age data of the Tangtse Pluton (the Muglib dome of Phillips and Searle, 2007) yielded 15.1 ± 0.6 Ma (Phillips and Searle, 2007). Other age results for leucogranite intrusions in the Tangtse area include 15.6 ± 0.1 Ma for a sample within the Tangtse Shear Zone (Phillips et al., 2004), 18.0 ± 0.6 Ma for a Grt–Ms–Bt-leucogranite sampled close to Tangtse (Searle et al., 1998), and between 16.6 ± 0.2 Ma and 19.1 ± 1.1 Ma from Ms–Bt-leucogranite samples collected close to Darbuk (Ravikant et al., 2009). A similar Ar–Ar age of 18 Ma was obtained for amphibole in an amphibolite sample from the Tangtse area (Rolland et al., 2009). Late-stage pegmatite dykes from the Tangtse Shear Zone yielded an even younger U–Pb zircon age of 13.7 ± 0.2 Ma (Phillips et al., 2004), but it is not clear whether these younger intrusions result from *in situ* melting of the anatectic rocks exposed in that area or whether they are intrusive rocks generated elsewhere. Due to the general spread in ages, we conclude that magmatism in the region lasted at least between 20 and 13.5 Ma and that the difference in ages found for the Tangtse Pluton (18.0 ± 0.4 Ma and 15.1 ± 0.6 Ma) indicates the duration of its growth.

The younger ages of leucogranites in the Karakoram Shear Zone are comparable to samples from the Karakoram Batholith. A leucogranite sample collected close to Satti in the Nubra Valley, NW

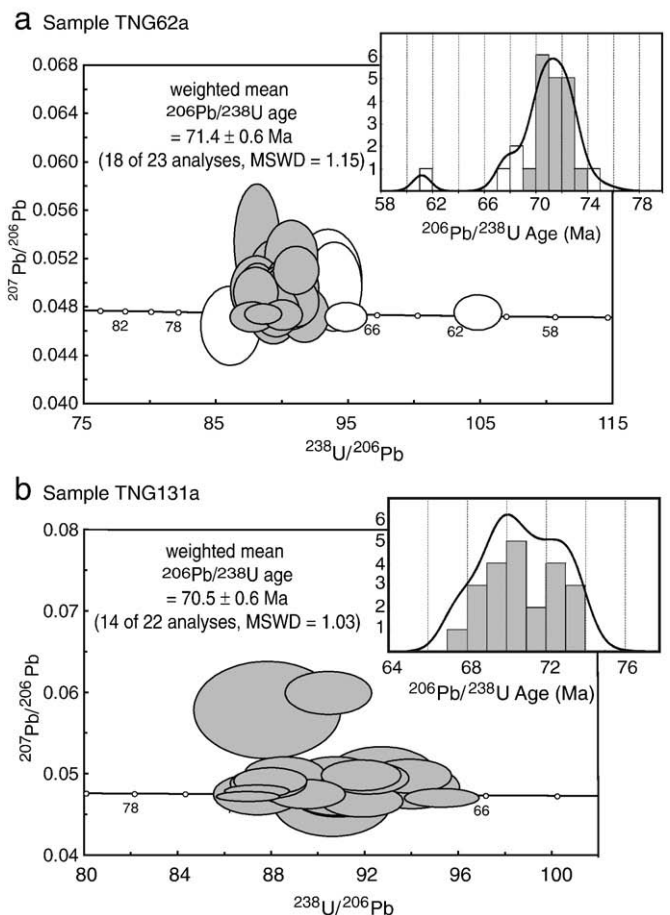


**Fig. 11.** Tera-Wasserburg concordia diagrams for sample TNG62a and sample TNG131a (Zrn). Inserts are histograms of relative age probability vs. number of spots in U–Pb SHRIMP analysis. Error ellipses are 68.3% confidence. (a) Zircons from the melanosome of a Hbl–Bt–granodiorite (sample TNG62a). (b) Zircons from a Bt–granodiorite (sample TNG131a).

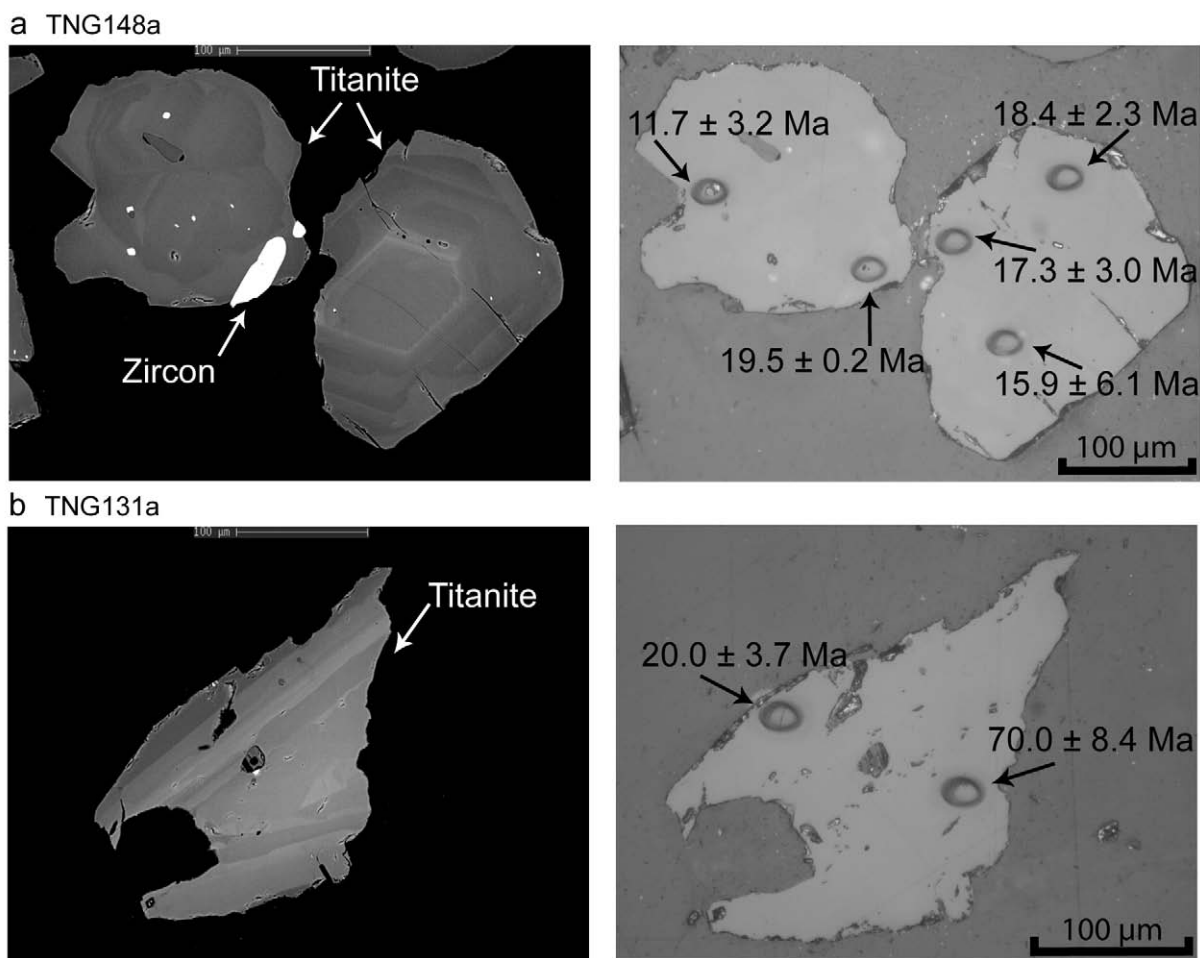


**Fig. 12.** (a) BSE image (left) and post-analysis photograph (right) of titanite grains from sample TNG148a. Note that the zircon inclusion yielded an older age than that of the surrounding titanite (see also Table 4). (b) BSE image (left) and post-analysis photograph (right) of a titanite grain from sample TNG131a. Ages are indicated for each analyzed spot (see also Table 3).

of the Pangong Metamorphic Complex, yielded a zircon SHRIMP crystallization age of  $15.0 \pm 0.4$  Ma (Weinberg et al., 2000), similar to a mylonitic leucogranite also from Satti (ID-TIMS zircon age  $15.9 \pm 0.1$  Ma; Phillips et al., 2004). A late-stage leucogranite dyke from this batholith collected further NW along strike of the Nubra Valley yielded ID-TIMS zircon age of  $13.7 \pm 0.3$  Ma (Phillips et al., 2004).

The crystallization ages of the calc-alkaline Muglib Batholith obtained here, at  $71.4 \pm 0.6$  Ma (sample TNG62a) and  $70.5 \pm 0.6$  Ma (sample TNG131a), overlap with a Rb–Sr age of  $72 \pm 8$  Ma (Ravikant, 2006) for a Hbl–Bt–granodiorite sample close to Muglib village, while Ravikant (2006) obtained a Rb–Sr age of  $118 \pm 15$  Ma for a migmatitic granodiorite in the Tangtse gorge. A U–Pb SHRIMP zircon age of  $68 \pm 1$  Ma was determined for the calc-alkaline Tirit granite at the confluence of the Shyok and Nubra Rivers by Weinberg et al. (2000). This suggests that a series of calc-alkaline bodies, possibly forming a continuous batholith that runs from Muglib along the Pangong Range and at the feet of the Saltoro Range in the Nubra Valley were emplaced between 67 and 72 Ma, possibly extending back to c. 120 Ma.

Titanite analyses of the Bt–granodiorite at the base of the Tangtse Pluton (Fig. 7b; sample TNG131a) yielded two age populations (Fig. 13c). The older group, 60–65 Ma, may represent early metamorphism in the Muglib Batholith, related to the heat from intrusion of late phases of calc-alkaline magmatism or, to slow cooling through the blocking temperature of titanite. The fact that the younger age range of ~11 to 21 Ma overlaps with the crystallization ages of the anatectic leucogranites of the Tangtse Pluton supports our interpretation that magma derived from anatexis of the Muglib Batholith contributed to form the Miocene leucogranite intrusions in the area.

This interpretation is further supported by the presence of  $63.0 \pm 0.8$  Ma zircon cores in Miocene leucogranites from Tangtse (Searle et al., 1998). In the same study, a migmatitic orthogneiss, probably related to the Muglib Batholith, showed two age groups. The older group with a mean weighted U–Pb age of  $106.3 \pm 2.3$  Ma was interpreted as the crystallization age of the orthogneiss, and the younger group with ages ranging between 22 and 15 Ma as the result of metamorphic growth during migmatization (Searle et al., 1998).

#### 9.4. Origin of the Muglib Batholith

Considering the temporal and compositional similarities between the Tirit granite and the Muglib Batholith, and the extent of our mapping in the region (Fig. 1), we suggest that a Cretaceous calc-alkaline body crops out semi-continuously for at least 85 km along the Karakoram Shear Zone: from SE of Muglib and northwestwards along the Pangong Range to the Nubra–Shyok confluence where it links with the Tirit granite along the northeastern side of the Saltoro Range (Weinberg et al., 2000). These magmatic rocks are also temporally, chemically and isotopically similar to the Ladakh Batholith which crops out immediately south of the Karakoram Shear Zone (Weinberg and Dunlap, 2000; Upadhyay et al., 2008; Ravikant et al., 2009).

The Ladakh Batholith resulted from subduction-related calc-alkaline magmatism which ceased as a result of the collision with India ca. 50 Ma (Schärer et al., 1984; Weinberg and Dunlap, 2000; Upadhyay et al., 2008). Crystallization ages range between 49 Ma and 103 Ma, broadly coincident with those determined for the Muglib–Tirit bodies with ages centered around 70 Ma. Ravikant et al.

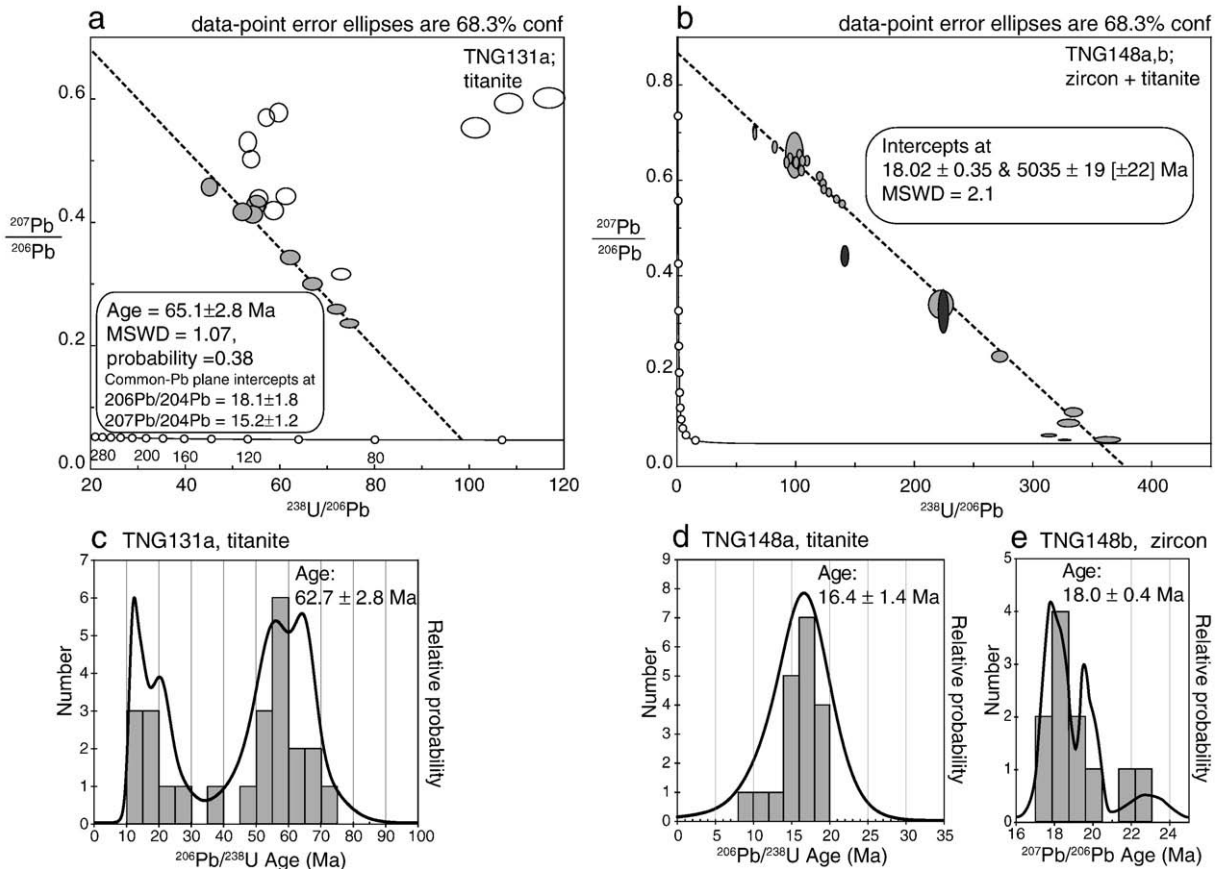


**Fig. 13.** (a) Concordia constrained linear 3-D isochron for sample TNG131a (Ttn). (b) Concordia diagram for samples TNG148a (Ttn) and TNG148b (Zrn) plotted together. (c) Histogram of titanite analyses of sample TNG131a. (d and e) Histogram of titanite and zircon analyses of samples TNG148a and TNG148b, respectively.

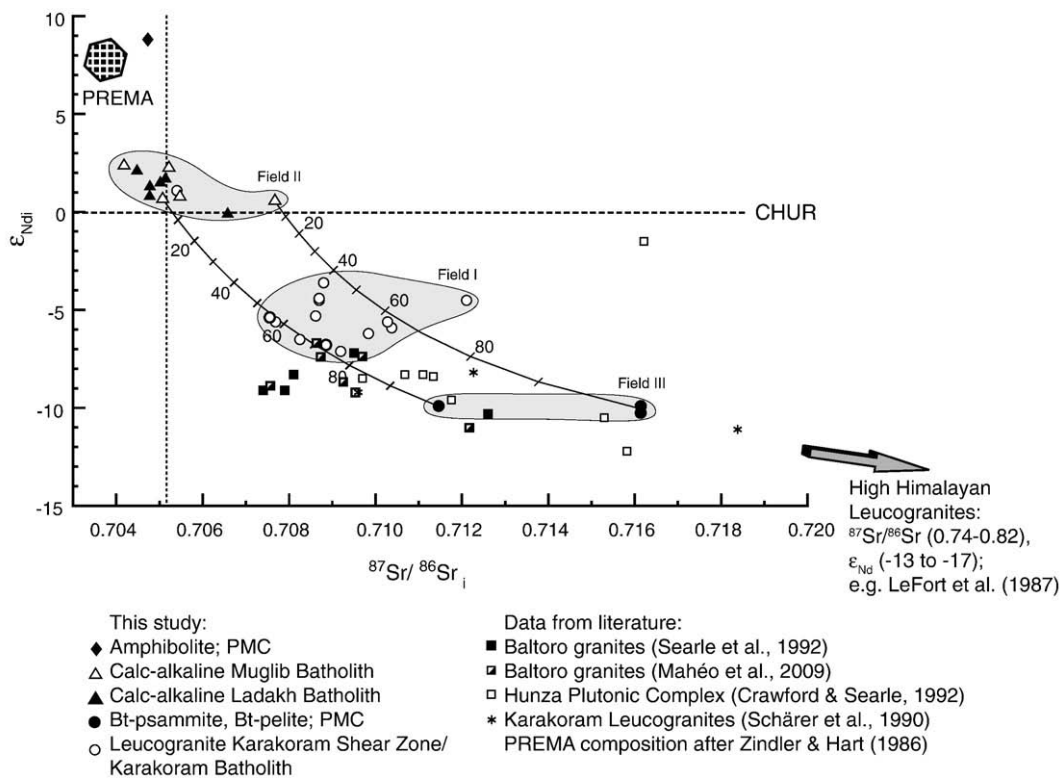


**Fig. 14.**  $^{87}\text{Sr}/^{86}\text{Sr}_i$  vs.  $\epsilon_{\text{Nd}i}$  diagram calculated at 18 Ma. Curves are calculated mixing lines between end-member isotopic compositions of calc-alkaline granitoids and meta-sedimentary rocks. The grey fields mark the range of isotopic compositions for leucogranites (field I) and source rocks (field II and III).

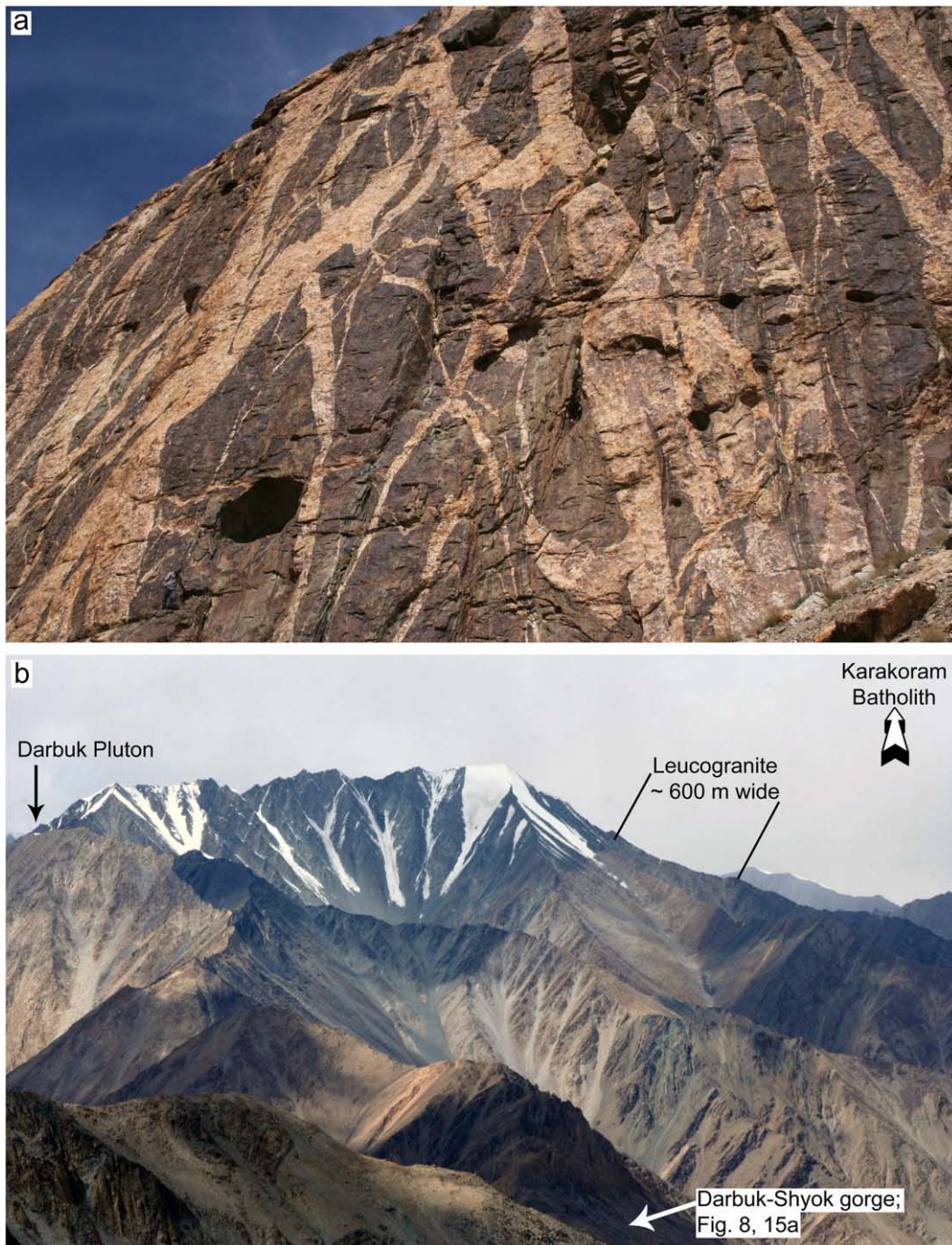


**Fig. 15.** Magma transport out of the source region. (a) Leucogranite dyke network in calc-silicate rocks the Darbuk–Shyok gorge. The dykes on this photo are up to ~5 m wide and merge and split seamlessly. Person on lower left of photograph as scale (below and left of shadow). (b) Pangong Range looking NW, showing an elongated leucogranite body 600 m thick (light band) that can also be seen in satellite images. Viewpoint is Pangong Range close to the Tangtse Pluton. The band can be followed into the Darbuk–Shyok gorge, where the dyke network in (a) and Fig. 8 are exposed (closer to viewer). The leucogranite pluton on the left hand side is connected to the dyke network. The far ridge of the leucogranite band is 15 km along strike from viewpoint.

(2009) concluded that the Ladakh Batholith formed in two magmatic stages, one between 83 and 103 Ma and the other between 50 and 67 Ma. The 67–72 Ma age of the Muglib Batholith and Tirit granite (Weinberg et al., 2000; Ravikant 2006) thus represent the upper end of the younger group. Calc-alkaline intrusions around 70 Ma are at odds with the model of ‘flat subduction’ of Neotethyan lithosphere that resulted in a cessation of magmatic activity at the South Tibetan margin in the period between 60 and 70 Ma (Wen et al., 2008). However, given the large distance to the study area in Ladakh, this

discrepancy might indicate diachronous changes along the subduction zone.

Both the Ladakh and Muglib Batholiths have an identical isotopic signature indicative of mantle derivation with only minor crustal influence, or derivation from crustal rocks that themselves have short crustal pre-histories. Based on these similarities we suggest that the calc-alkaline Muglib Batholith, including the Tirit granite, and the Ladakh Batholith are effectively part of the same island arc, developed south of the Asian margin.

## 9.5. Linking source to sink

### 9.5.1. Field relations

In migmatites of the Tangtse gorge region, layer-parallel leucosomes in folds merge with axial planar leucosomes thus forming an interconnected melt flow network and demonstrating contemporaneity of anatexis with folding and shearing (Weinberg and Mark 2008). The network that arises allows for contemporaneous migration and mixing of magmas from different sources as demonstrated by the features documented at the base of the Tangtse Pluton (Fig. 7) and the Darbuk–Shyok gorge (Fig. 8), and supported by the isotope systematics (Fig. 14).

Moving up from outcrop scale, an interconnected network of leucogranite sheets, each several meters wide, is well developed in interlayered amphibolites and calc-silicate rocks hundreds of meters wide at the SW end of the Tangtse gorge and in the Darbuk–Shyok gorge over 13 km along strike (Fig. 15a). A large-scale network is also developed in the anatectic calc-alkaline and meta-sedimentary rocks, but is much more irregular in terms of sheet orientations and widths (see also the Pangong Injection Complex of Weinberg and Searle, 1998). We interpret these networks as large-scale magma pathways through both anatectic and non-anatectic rocks.

This system of intrusive sheets is related to a number of kilometer-sized leucogranite plutons in the Karakoram Shear Zone, such as the Tangtse and Darbuk Plutons (Fig. 1b, 2) and the ~600 m wide sheeted body through the centre of the Pangong Range in Fig. 15b. The anastomosing sheet network, plutons and sheeted bodies are together interpreted as the magma transfer zone between the source and the Karakoram Batholith that crops out to the NW of the Pangong Range (Fig. 15b). This interpretation is supported by our mapping closer to the Karakoram Batholith and by isotopic similarity from the source all the way to the Karakoram Batholith. At Agham, further NW of the Tangtse–Darbuk area and at the southern tip of the Karakoram Batholith, leucogranite dykes partly retrogressed to greenschist facies, intrude strongly deformed chlorite and muscovite schists as well as gabbroic rocks of the Muglib Batholith. Leucogranites here have the same isotopic composition as in the source area (sample AGH25a, Table 5). Further NW, the exposed contact between the Karakoram Batholith and its footwall in Rongdu is characterized by a network of mylonitized leucogranite sheets. Thus, sheets of essentially similar leucogranites can be followed from their source in the Pangong Range to the Karakoram Batholith over 80 km along strike.

This link between the source zone and the batholith is further supported by the presence of a kilometer-wide zone of Hbl-bearing leucogranites, including partly disrupted decimetric to metric enclaves of migmatitic Hbl–Cpx–diortite inside the Karakoram Batholith near Rongdu. These Hbl-bearing leucogranites are similar to those documented in the source region near Muglib, and the migmatitic diortite enclaves are similar to the anatectic diortites of the Muglib Batholith and are interpreted to represent blocks of the migmatitic source. As seen above, the leucosomes in these diortitic enclaves yielded a hybrid signature similar to the rest of the Karakoram Batholith, rather than the pure signature of the Muglib Batholith (sample AGH23a, Table 5).

Along the NE-side of the Nubra Valley, the Karakoram Batholith is emplaced in greenschist facies meta-sedimentary rocks and meta-volcanic rocks (e.g. Weinberg et al. 2000; Phillips et al., 2004), and thus exposes a higher structural crustal level than the deeply exhumed upper amphibolite facies rocks of the PMC. Interestingly, the width of the Karakoram Batholith, as partly interpreted from satellite images, is similar to the width of the Pangong Range measured between the Tangtse and the Pangong shear zones (Figs. 1, 2). If the Karakoram Batholith intruded synkinematically (Mahéo et al., 2004) as has also been demonstrated for the Tangtse Pluton and other leucogranites along the Karakoram Fault (Lacassin et al., 2004; Rolland et al. 2009; Weinberg et al., 2009), its measured displacement does not measure the full displacement on the Karakoram Shear Zone.

The southernmost tip of the Karakoram Batholith currently crops out ~40 km from the northernmost significant migmatite area in the Darbuk–Shyok gorge (Fig. 1a, b). Given the dextral movement on the shear zone, the Karakoram Batholith in Ladakh would have been further away from the migmatite area at the time of anatexis. The link between the anatectic rocks exposed in the PMC and the Karakoram Batholith demonstrated here does not necessarily imply that voluminous magma from this particular source found its way to the now exposed batholith, but rather suggests that the Karakoram Batholith was fed mostly from a source similar to the one exposed in the PMC.

### 9.5.2. Implications of the isotopic signatures

Initial  $^{87}\text{Sr}/^{86}\text{Sr}$  and  $\varepsilon_{\text{Nd}i}$  values of the leucogranites and leucosomes from the Pangong Range are intermediate between those of the meta-sedimentary rocks of the Pangong Metamorphic Complex and the Muglib Batholith, the likely magma sources. In the  $^{87}\text{Sr}/^{86}\text{Sr}_i$  vs.  $\varepsilon_{\text{Nd}i}$  diagram (Fig. 14), these intermediate values lie in a field defined by hyperbolic mixing curves between representative end-member compositions. It is interesting to notice that leucosomes, interpreted to be roughly *in situ*, also have mixed signatures (samples TNG71a, TNG131g; Table 5). The only exception is a tonalitic leucosome sample (sample TNG170, Table 5) from a metatexite migmatite in the central part of the Tangtse gorge. It yields isotopic values similar to a patchy melanosome in diortite (sample TNG169a) in the same outcrop and also to other samples of the Muglib Batholith. These findings suggest that in general, mixing occurred at an early stage in the migration history of the magmas.

These hybrid leucogranites exposed close to the source have similar values to those in intrusive sheets or plutons in the vicinity, as well as to those of the Karakoram Batholith (samples AGH25a, NBR1b, NBR2a and NBR3b in Table 5) supporting our field-based interpretation that the system is effectively connected from the source in the Pangong Range to the Karakoram Batholith. This is further supported by Hf isotope data, which suggest a similar origin for the leucogranites

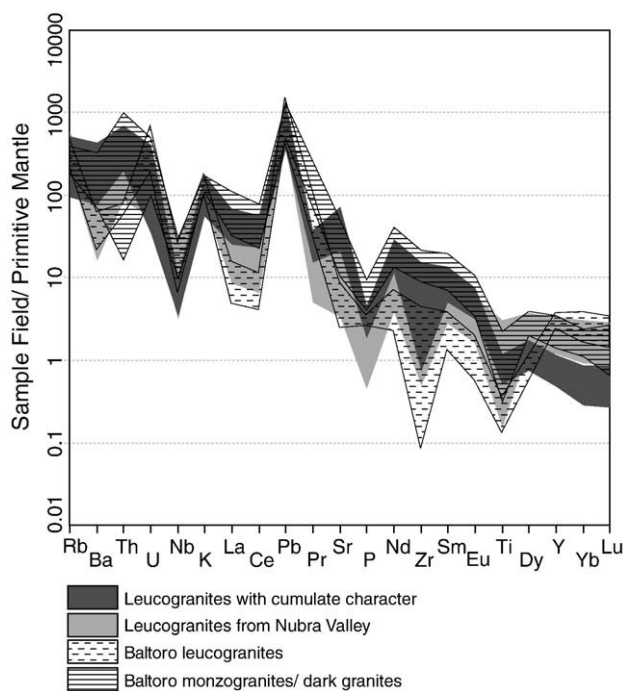


Fig. 16. Comparison of averaged subsets of leucogranite samples to available data for Baltoro granites. Samples are normalized to primitive mantle composition (Sun and McDonough, 1989). Leucogranites with cumulate character (high Sr and Ba):  $N=9$ ; leucogranites from Nubra Valley:  $N=9$ ; Baltoro leucogranites:  $N=5$  (Searle et al., 1992); Baltoro monzogranites:  $N=4$  (Searle et al., 1992); Baltoro dark granites:  $N=5$  (Debon et al., 1986; Mahéo et al., 2002).

in the Karakoram Shear Zone and granitoids of similar ages of the Karakoram Batholith (Ravikant et al., 2009). We therefore conclude that magmas derived from the meta-sedimentary sequence and the calc-alkaline Muglib Batholith mixed early in their migration, and that this mixed magma gave rise to the Karakoram Batholith.

#### 9.6. Similar leucogranite intrusions elsewhere in the Karakoram?

The Hunza Plutonic Unit and the Baltoro Batholith in Pakistan mark the NW continuation of the Karakoram Batholith (Crawford and Windley, 1990; Searle et al., 1992; Searle et al., 1998; Srimal, 1986). The Baltoro Batholith is mostly composed of Bt ± Ms ± Grt-monzogranites and leucogranites that show mineralogical and geochemical similarities to the leucogranites of the Karakoram Shear Zone and the Karakoram Batholith (Searle et al., 1992), and are only slightly older (U–Pb zircon age  $21 \pm 0.5$  Ma; Parrish and Tirrul, 1989). Trace element concentrations of our granites compare well to those of the Baltoro granite (Fig. 16; Crawford and Windley, 1990; Mahéo et al., 2009), suggesting a genetic link across the Pakistan–India border and across the Karakoram Shear Zone. Comparison of isotopic data in Fig. 14 further supports this link. Here we have included isotope data for the Karakoram and Baltoro granites, and granites of the Hunza Plutonic Unit from previous studies. Some of the Baltoro and Hunza samples overlap with our data, but others tend to show lower  $\epsilon_{\text{Nd}}$  and some samples show higher  $^{87}\text{Sr}/^{86}\text{Sr}_i$  values.

The isotope data for the Hunza and Baltoro granitoids can be explained using the same two source rocks inferred to have produced the Karakoram Batholith, but require more input from the meta-sedimentary sequence carrying the crustal signature. Whilst the Karakoram Batholith requires 40–70 % input from magmas derived from the meta-sedimentary rocks, the Hunza and Baltoro granitoids require more than 70 %. Exceptions are samples from Karakoram granites in Pakistan that show an even stronger crustal signature. Schärer et al. (1990) proposed, based on zircon and monazite inheritance and Pb, Sr and Nd isotopes that likely sources of these granites are the meta-sedimentary rocks of the Karakoram Metamorphic Complex in that region.

Alternative sources for the origin of the isotopic signature of granites in the Hunza and Baltoro areas have been suggested by Mahéo et al. (2002) and Mahéo et al. (2009). These include melting of metasomatized mantle in which melting was induced by asthenospheric upwelling after an inferred slab break-off of the subducted Indian plate, at the time of magmatism in the Karakoram and South Tibet. This component is indicated by the presence of lamprophyres cropping out in the area and which would have provided the heat for crustal melting or mixed with other magma sources to produce the leucogranites (Mahéo et al., 2009). Further, Mahéo et al. (2009) proposed partial melting of Cretaceous, calc-alkaline mafic to dioritic lower crust to account for the Baltoro granitic magmatism.

Multiple alternatives may be and have been proposed for interpreting essentially the same isotopic signatures. We argue that field relations allow us to directly document the process of magma generation and migration from the anatectic terrane exposed in the Pangong Metamorphic Complex, comprising a Late Cretaceous island arc batholith and its meta-sedimentary country rocks, to the Miocene leucogranites of the Karakoram Batholith.

## 10. Conclusions

In the Karakoram Shear Zone, anatexis of Late Cretaceous calc-alkaline granodiorites and diorites of the Muglib Batholith and of meta-sedimentary rocks of the Pangong Metamorphic Complex took place during deformation and as a result of water-fluxed melting. Magmas from this heterogeneous source formed an extensive network of channels, across a number of scales, which allowed for

extraction. The initial  $^{87}\text{Sr}/^{86}\text{Sr}$  and  $\epsilon_{\text{Nd}}$  values of leucosomes, leucogranite sheets, stocks and plutons in the Karakoram Shear Zone are similar to those of the Karakoram Batholith and vary between 0.7086 to 0.7121 and  $-7.1$  to  $-3.6$ , respectively. This is a hybrid signature between the two sources identified in the anatectic zone. We conclude therefore that the Karakoram Batholith is a result of melting of a heterogeneous source in the presence of a water-rich fluid, and that the mixing of these different magmas took place already within the source region.

## Acknowledgements

We would like to thank Yann Rolland and Vadlamani Ravikant for constructive reviews and Olav Eklund for handling of the paper in the editing process. We also thank Bruce Schaefer for helpful discussions on isotope geochemistry, Roland Maas for carrying out isotope analysis, as well as Massimo Raveggi for help with ICP-MS analysis. This paper is part of the PhD thesis of the first author.

## Appendix A. Supplementary data

Supplementary data associated with this article can be found, in the online version, at doi:10.1016/j.lithos.2009.11.013.

## References

- Aleinikoff, J.N., Wintsch, R.P., Tollo, R.P., Unruh, D.M., Fanning, C.M., Schmitz, M.D., 2007. Ages and origins of rocks of the Killingworth Dome, south-central Connecticut; implications for the tectonic evolution of southern New England. *American Journal of Science* 307 (1), 63–118.
- Andersson, U.B., 1991. Granitoid episodes and mafic/felsic magma interaction in the Svecofennian of the Fennoscandian Shield, with main emphasis on the approximately 1.8 Ga plutonics. *Precambrian Research* 51 (1–4), 127–149.
- Andersson, U.B., Neymark, L.A., Billström, K., 2002. Petrogenesis of Mesoproterozoic (Subjotnian) rapakivi complexes of central Sweden; implications from U–Pb zircon ages, Nd, Sr and Pb isotopes. *Transactions of the Royal Society of Edinburgh: Earth Sciences* 92 (3–4), 201–228.
- Arth, J.G., 1976. Behavior of trace elements during magmatic processes; a summary of theoretical models and their applications. *Journal of Research of the U. S. Geological Survey* 4 (1), 41–47.
- Beard, J.S., Ragland, P.C., Crawford, M.L., 2005. Reactive bulk assimilation; a model for crust–mantle mixing in silicic magmas. *Geology* 33 (8), 681–684.
- Berger, A., Burri, T., Alt-Epping, P., Engi, M., 2008. Tectonically controlled fluid flow and water-assisted melting in the middle crust: an example from the Central Alps. *Lithos* 102 (3–4), 598–615.
- Black, L.P., Kamo, S.L., Allen, C.M., Aleinikoff, J.N., Davis, D.W., Korsch, R.J., Foudoulis, C., 2003. TEMORA 1; a new zircon standard for Phanerozoic U–Pb geochronology. *Chemical Geology* 200 (1–2), 155–170.
- Brown, E.T., Bendick, R., Bourles, D.L., Gaur, V., Molnar, P., Raisbeck, G.M., Yiou, F., 2002. Slip rates of the Karakoram fault, Ladakh, India, determined using cosmic ray exposure dating of debris flows and moraines. *Journal of Geophysical Research B: Solid Earth* 107 (9), 1–7.
- Burri, T., Berger, A., Engi, M., 2005. Tertiary migmatites in the Central Alps: regional distribution, field relations, conditions of formation and tectonic implications. *Schweizerische Mineralogische und Petrographische Mitteilungen* 85 (2–3), 215–232.
- Clemens, J.D., 2006. Melting of the continental crust; fluid regimes, melting reactions, and source rock fertility. In: Brown, M., Rushmer, T. (Eds.), *Evolution and Differentiation of the Continental Crust*. Cambridge University Press, New York, NY, United States, pp. 296–330.
- Clemens, J.D., Vielzeuf, D., 1987. Constraints on melting and magma production in the crust. *Earth and Planetary Science Letters* 86 (2–4), 287–306.
- Crawford, M.B., Searle, M.P., 1992. Field relationships and geochemistry of pre-collisional (India–Asia) granitoid magmatism in the central Karakoram, northern Pakistan. *Tectonophysics* 206 (1–2), 171–192.
- Crawford, M.B., Windley, B.F., 1990. Leucogranites of the Himalaya/Karakoram: implications for magmatic evolution within collisional belts and the study of collision-related leucogranite petrogenesis. *Journal of Volcanology and Geothermal Research* 44 (1–2), 1–19.
- Debon, F., Zimmermann, J.L., Bertrand, J.M., 1986. Le granite du Baltoro (batholite axiale du Karakorum, nord Pakistan): une intrusion subalcaline d'âge Miocène Supérieur. *Comptes Rendus de l'Académie des Sciences, Paris, Série II* 303 (6), 463–468.
- Deniel, C., Vidal, P., Fernandez, A., Le Fort, P., Peucat, J.J., 1987. Isotopic study of the Manaslu granite (Himalaya, Nepal); inference on the age and source of Himalayan leucogranites. *Contributions to Mineralogy and Petrology* 96 (1), 78–92.
- Dunlap, W.J., Weinberg, R.F., Searle, M.P., 1998. Karakoram fault zone rocks cool in two phases. *Journal of the Geological Society* 155 (6), 903–912.
- Eggins, S.M., Woodhead, J.D., Kinsley, L.P.J., Mortimer, G.E., Sylvester, P., McCulloch, M.T., Hergt, J.M., Handler, M.R., 1997. A simple method for the precise determination of



- >=40 trace elements in geological samples by ICPMS using enriched isotope internal standardisation. *Chemical Geology* 134 (4), 311–326.
- Gardien, V., Thompson, A.B., Ulmer, P., 2000. Melting of biotite + plagioclase + quartz gneisses; the role of H (sub 2) O in the stability of amphibole. *Journal of Petrology* 41 (5), 651–666.
- Genier, F., Bussy, F., Epard, J.-L., Baumgartner, L., 2008. Water-assisted migmatization of metagraywackes in a Variscan shear zone, Aiguilles-Rouges massif, western Alps. *Lithos* 102 (3–4), 575–597.
- Guillot, S., Le Fort, P., 1995. Geochemical constraints on the bimodal origin of High Himalayan leucogranites. *Lithos* 35 (3–4), 221–234.
- Hawkesworth, C.J., Vollmer, R., 1979. Crustal contamination versus enriched mantle:  $^{143}\text{Nd}/^{144}\text{Nd}$  and  $^{87}\text{Sr}/^{86}\text{Sr}$  evidence from the Italian volcanics. *Contributions to Mineralogy and Petrology* 69 (2), 151–165.
- Holtz, F., Pichavant, M., Barbey, P., Johannes, W., 1992. Effects of H (sub 2) O on liquidus phase relations in the haplogranite system at 2 and 5 kbar. *American Mineralogist* 77 (11–12), 1223–1241.
- Honegger, K., Dietrich, V., Frank, W., Gansser, A., Thöni, M., Trommsdorff, V., 1982. Magmatism and metamorphism in the Ladakh Himalayas (the Indus–Tsangpo suture zone). *Earth and Planetary Science Letters* 60, 253–292.
- Inger, S., Harris, N., 1993. Geochemical constraints on leucogranite magmatism in the Langtang Valley, Nepal Himalaya. *Journal of Petrology* 34 (2), 345–368.
- Jade, S., Bhatt, B.C., Yang, Z., Gaur, V.K., Molnar, P., Anand, M.B., Kumar, D., 2004. GPS measurements from the Ladakh Himalaya, India: preliminary tests of plate-like or continuous deformation in Tibet. *Geological Society of America Bulletin* 116, 1385–1391.
- Kenah, C., Hollister, L.S., 1983. Anatexis in the Central Gneiss Complex. In: Atherton, M.P., Gribble, C.D. (Eds.), *Migmatites, Melting, and Metamorphism*. Shiva, Nantwich, pp. 142–162.
- Kretz, R., 1983. Symbols for rock-forming minerals. *American Mineralogist* 68, 277–279.
- Lacassin, R., Valli, F., Arnod, N., Leloup, P.H., Paquette, J.L., Haibling, L., Tapponnier, P., Chevalier, M.-L., Guillot, S., Mahéo, G., Zhiqin, X., 2004. Large-scale geometry, offset and kinematic evolution of the Karakorum Fault, Tibet. *Earth and Planetary Science Letters* 219, 255–269.
- Lappin, A.R., Hollister, L.S., 1980. Partial melting in the Central Gneiss Complex near Prince Rupert, British Columbia. *American Journal of Science* 280 (6), 518–545.
- Le Fort, P., Cuney, M., Deniel, C., France-Lanord, C., Sheppard, S.M.F., Upreti, B.N., Vidal, P., 1987. Crustal generation of the Himalayan leucogranites. *Tectonophysics* 134 (1–3), 39–57.
- Ludwig, K.R., 2001. SQUID 1.02, A user's manual. Berkeley Geochronology Center Special Publication 2.
- Ludwig, K.R., 2003. User's manual for Isoplot/Ex, Version 3.0, A geochronological toolkit for Microsoft Excel. Berkeley Geochronology Center Special Publication 4.
- Maas, R., Kamenetsky, M.B., Sobolev, A.V., Kamenetsky, V.S., Sobolev, N.V., 2005. Sr, Nd, and Pb isotope evidence for a mantle origin of alkali chlorides and carbonates in the Udachnaya Kimberlite, Siberia. *Geology* 33 (7), 549–552.
- Maas, R., McCulloch, M.T., 1991. The provenance of Archean clastic metasediments in the Narryer Gneiss Complex, Western Australia: trace element geochemistry, Nd isotopes, and U–Pb ages for detrital zircons. *Geochimica et Cosmochimica Acta* 55 (7), 1915–1932.
- Mahéo, G., Blichert-Toft, J., Pin, C., Guillot, S., Pêcher, A., 2009. Partial melting of mantle and crustal sources beneath South Karakorum, Pakistan: implications for the Miocene geodynamic evolution of the India–Asia convergence zone. *Journal of Petrology* 50 (3), 427–449.
- Mahéo, G., Guillot, S., Blichert-Toft, J., Rolland, Y., Pêcher, A., 2002. A slab breakoff model for the Neogene thermal evolution of South Karakorum and South Tibet. *Earth and Planetary Science Letters* 195 (1–2), 45–58.
- Mahéo, G., Pêcher, A., Guillot, S., Rolland, Y., Delacourt, C., 2004. Exhumation of Neogene gneiss domes between oblique crustal boundaries in south Karakorum, northwest Himalaya, Pakistan. *Special Paper – Geological Society of America* 380, 141–154.
- McLellan, E.L., 1988. Migmatite structures in the Central Gneiss Complex, Boca de Quadra, Alaska. *Journal of Metamorphic Geology* 6 (4), 517–542.
- Mogk, D.W., 1992. Ductile shearing and migmatization at mid-crustal levels in an Archean high-grade gneiss belt, northern Gallatin Range, Montana, USA. *Journal of Metamorphic Geology* 10 (3), 427–438.
- Parrish, R.R., Tirrul, R., 1989. U–Pb age of the Baltoro granite, northwest Himalaya, and implications for monazite U–Pb systematics. *Geology* 17 (12), 1076–1079.
- Patiño Douce, A.E., Harris, N., 1998. Experimental constraints on Himalayan anatexis. *Journal of Petrology* 39 (4), 689–710.
- Phillips, R.J., Parrish, R.R., Searle, M.P., 2004. Age constraints on ductile deformation and long-term slip rates along the Karakorum fault zone, Ladakh. *Earth and Planetary Science Letters* 226, 305–319.
- Phillips, R.J., Searle, M.P., 2007. Macrostructural and microstructural architecture of the Karakorum fault; relationship between magmatism and strike-slip faulting. *Tectonics* 26 (3) art. no. TC3017.
- Raczek, I., Jochum, K.P., Hofmann, A.W., 2003. Neodymium and strontium isotope data for USGS reference materials BCR-1, BCR-2, BHVO-1, BHVO-2, AGV-1, AGV-2, GSP-1, GSP-2 and eight MPI-DING reference glasses. *Geostandards Newsletter* 27 (2), 173–179.
- Ravikant, V., 2006. Utility of Rb–Sr geochronology in constraining Miocene and Cretaceous events in the eastern Karakorum, Ladakh, India. *Journal of Asian Earth Sciences* 27 (4), 534–543.
- Ravikant, V., Wu, F.-Y., Ji, W.-Q., 2009. Zircon U–Pb and Hf isotopic constraints on petrogenesis of the Cretaceous–Tertiary granites in eastern Karakorum and Ladakh, India. *Lithos* 110 (1–4), 153–166.
- Raz, U., Honegger, K., 1989. Magmatic and tectonic evolution of the Ladakh Block from field studies. *Tectonophysics* 161, 107–118.
- Rex, A.J., Searle, M.P., Tirrul, R., Crawford, M.B., Prior, D.J., Rex, D.C., Barnicoat, A.C., 1988. The geochemical and tectonic evolution of the central Karakorum, North Pakistan. *Philosophical Transactions of the Royal Society of London, Series A: Mathematical and Physical Sciences* 326 (1589), 229–255.
- Rolland, Y., Picard, C., Pêcher, A., Lapiere, H., Bosch, D., Keller, F., 2002. The Cretaceous Ladakh arc of NW Himalaya-slab melting and melt–mantle interaction during fast northward drift of Indian Plate. *Chemical Geology* 182 (2–4), 139–178.
- Rolland, Y., Mahéo, G., Pêcher, A., Villa, I.M., 2009. Syn-kinematic emplacement of the Pangong metamorphic and magmatic complex along the Karakorum Fault (N Ladakh). *Journal of Asian Earth Sciences* 34 (1), 10–25.
- Rolland, Y., Pêcher, A., 2001. The Pangong granulites of the Karakorum Fault (western Tibet); vertical extrusion within a lithosphere-scale fault? *Comptes Rendus de l'Académie des Sciences, Serie II, Sciences de la Terre et des Planètes* 332 (6), 363–370.
- Rollinson, H.R., 1993. *Using geochemical data; evaluation, presentation, interpretation*. Longman Scientific & Technical, Harlow, United Kingdom. 352 pp.
- Rutter, E.H., Faulkner, D.R., Brodie, K.H., Phillips, R.J., Searle, M.P., 2007. Rock deformation processes in the Karakorum fault zone, Eastern Karakorum, Ladakh, NW India. *Journal of Structural Geology* 29 (8), 1315–1326.
- Sawyer, E.W., 2008. *Atlas of migmatites*. The Canadian Mineralogist. Special Publication, Mineralogical Association of Canada, Ottawa, ON, Canada. 371 pp.
- Schärer, U., Copeland, P., Harrison, T.M., Searle, M.P., 1990. Age, cooling history, and origin of post-collisional leucogranites in the Karakorum Batholith; a multi-system isotope study. *Journal of Geology* 98 (2), 233–251.
- Schärer, U., Hamet, J., Allègre, C.J., 1984. The Transhimalaya (Gangdese) plutonism in the Ladakh region: a U–Pb and Rb–Sr study. *Earth and Planetary Science Letters* 67 (3), 327–339.
- Searle, M.P., Crawford, M.B., Rex, A.J., 1992. Field relations, geochemistry, origin and emplacement of the Baltoro granite, Central Karakorum. *Transactions of the Royal Society of Edinburgh: Earth Sciences* 83, 519–538.
- Searle, M.P., Tirrul, R., 1991. Structural and thermal evolution of the Karakorum crust. *Journal of the Geological Society of London* 148 (1), 65–82.
- Searle, M.P., Weinberg, R.F., Dunlap, W.J., 1998. Transpressional tectonics along the Karakorum Fault Zone, northern Ladakh. In: R.E. Holdsworth and R.A. Strachan (Editors), *Continental Transpressional and Transtensional Tectonics*. Geological Society of London Special Publication 135, 307–326.
- Srimal, N., 1986. India–Asia collision: implications for the geology of the eastern Karakorum. *Geology* 14, 523–527.
- Sun, S.S., McDonough, W.F., 1989. Chemical and isotopic systematics of oceanic basalts; implications for mantle composition and processes. *Geological Society of London Special Publication* 42, 313–345.
- Tanaka, T., Togashi, S., Kamioka, H., Amakawa, H., Kagami, H., Hamamoto, T., Yuhara, M., Orihashi, Y., Yoneda, S., Shimizu, H., Kunimaru, T., Takahashi, K., Yanagi, T., Nakano, T., Fujimaki, H., Shinjo, R., Asahara, Y., Tanimizu, M., Dragusanu, C., 2000. JNDI-1: a neodymium isotopic reference in consistency with LaJolla neodymium. *Chemical Geology* 168 (3–4), 279–281.
- Tera, F., Wasserburg, G.J., 1972. U–Th–Pb systematics in three Apollo 14 basalts and the problem of initial Pb in lunar rocks. *Earth and Planetary Science Letters* 14 (3), 281–304.
- Upadhyay, R., Frisch, W., Siebel, W., 2008. Tectonic implications of new U–Pb zircon ages of the Ladakh Batholith, Indus suture zone, northwest Himalaya, India. *Terra Nova* 20 (4), 309–317.
- Valli, F., Arnaud, N., Leloup, P.H., Sobel, E.R., Mahéo, G., Lacassin, R., Guillot, S., Li, H., Tapponnier, P., Xu, Z., 2007. Twenty million years of continuous deformation along the Karakorum fault, western Tibet: a thermochronological analysis. *Tectonics* 26 (4) art. no. TC4004.
- Vance, D., Thirlwall, M., 2002. An assessment of mass discrimination in MC-ICPMS using Nd isotopes. *Chemical Geology* 185 (3–4), 227–240.
- Weinberg, R.F., Dunlap, W.J., 2000. Growth and deformation of the Ladakh Batholith, Northwest Himalayas; implications for timing of continental collision and origin of calc-alkaline batholiths. *Journal of Geology* 108 (3), 303–320.
- Weinberg, R.F., Dunlap, W.J., Whitehouse, M., 2000. New field, structural and geochronological data from the Shyok and Nubra valleys, northern Ladakh: linking Kohistan to Tibet. In: A. Khan, P.J. Treloar and M.P. Searle (Eds.), *Tectonics of the Nanga Parbat Syntaxis and the Western Himalaya*. Geological Society of London Special Publication 170, 253–275.
- Weinberg, R.F., Mark, G., 2008. Magma migration, folding, and disaggregation of migmatites in the Karakorum shear zone, Ladakh, NW India. *Geological Society of America Bulletin* 120 (7–8), 994–1009.
- Weinberg, R.F., Mark, G., Reichardt, H., 2009. Magma ponding in the Karakorum shear zone, Ladakh, NW India. *Geological Society of America Bulletin* 121 (1–2), 278–285.
- Weinberg, R.F., Searle, M.P., 1998. The Pangong Injection Complex, Indian Karakorum: a case of pervasive granite flow through hot viscous crust. *Journal of the Geological Society of London* 155 (5), 883–891.
- Wen, D.-R., Liu, D., Chung, S.-L., Chu, M.-F., Ji, J., Zhang, Q., Song, B., Lee, T.-Y., Yeh, M.-W., Lo, C.-H., 2008. Zircon SHRIMP U–Pb ages of the Gangdese Batholith and implications for Neotethyan subduction in southern Tibet. *Chemical Geology* 252 (3–4), 191–201.
- Williams, I.S., 1998. U–Th–Pb geochronology by ion microprobe. *Reviews in Economic Geology* 7, 1–35.
- Williams, I.S., Hergt, J.M., 2000. U–Pb dating of Tasmanian dolerites; a cautionary tale of SHRIMP analysis of high-U zircon. *Beyond 2000. New Frontiers in Isotope Geoscience* 185–188.
- Wright, T.J., Parsons, B., England, P.C., Fielding, E.J., 2004. InSAR observations of low slip rates on the major faults of western Tibet. *Science* 305 (5681), 236–239.
- Zindler, A., Hart, S.R., 1986. *Chemical geodynamics*. *Annual Review of Earth and Planetary Sciences* 14, 493–571.